# Fatigue design of welded double-sided T-joints and double-sided cruciform joints in steel marine structures

## A total stress concept

Qin, Yanxin; den Besten, Henk; Palkar, Saloni; Kaminski, Miroslaw Lech

**DOI**
10.1111/ffe.13089

**Publication date**
2019

**Document Version**
Final published version

**Published in**
Fatigue and Fracture of Engineering Materials and Structures

Received: 11 April 2019 | Revised: 27 May 2019 | Accepted: 7 June 2019

DOI: 10.1111/ffe.13089

ORIGINAL CONTRIBUTION

WILEY

# Fatigue design of welded double-sided T-joints and double-sided cruciform joints in steel marine structures: A total stress concept

**Yanxin Qin** | **Henk den Besten** | **Saloni Palkar** | **Miroslaw Lech Kaminski**

Maritime and Transport Technology Department, Delft University of Technology, Delft, The Netherlands

**Correspondence**
Henk den Besten, Maritime and Transport Technology Department, Delft University of Technology, Delft, The Netherlands.
Email: Henk.denBesten@tudelft.nl

**Funding information**
China Scholarship Council, Grant/Award Number: 201606950015

**Abstract**

Fatigue is a governing design limit state for marine structures. Welded joints are important in that respect. The weld notch stress (intensity) distributions contain essential information and formulations have been established to obtain a total stress fatigue damage criterion and corresponding fatigue resistance curve; a total stress concept. However, the involved weld load carrying stress model does not provide the required estimates and trends for varying geometry dimensions and loading & response combinations. A new one has been developed and performance evaluation for T-joints and cruciform joints in steel marine structures shows that in comparison with the nominal stress, hot spot structural stress and effective notch stress concept based results up to 50% more accurate fatigue design life time estimates can be obtained. Taking advantage of the weld notch stress formulations, the effective notch stress concept performance has improved adopting a stress-averaged criterion rather than a fictitious notch radius-based one.

**KEYWORDS**

fatigue design, joint resistance curve, steel marine structures, total stress criterion, welded double-sided cruciform joints, welded double-sided T-joints

## 1 | INTRODUCTION

Marine structures active in inland, coastal, offshore and deep-sea waters are exposed to cyclic mechanical loading, both environment (wind and waves) and service (operations and machinery) induced. The response is cyclic by nature accordingly, meaning fatigue, a cyclic loading & response induced local, progressive, structural damage process,[1] is a governing limit state. Investigations for marine structures like oil tankers,[2] container ships,[3] bulk carriers,[4] cruise ships,[5] ferries[6] and planing crafts[7] reflect the importance.

Fatigue-sensitive locations, hot spots, emerge at notched geometries either as part of structural members (e.g. cut-outs) or at structural member connections (e.g. joints). Since marine structures are traditionally structural member assemblies in stiffened panel, truss, or frame set-up, particular attention is paid to arc-welded joints typically

**NOMENCLATURE:** FE, finite element; HCF, high cycle fatigue, life time range $N = O(5 \cdot 10^6 \sim 10^9)$ cycles; LCB, lower confidence bound; MCF, medium cycle fatigue, life time range $N = O(10^4 \sim 5 \cdot 10^6)$ cycles; MLE, maximum likelihood estimate; (N)LC, (non-)load carrying; UCB, upper confidence bound.

connecting the structural members. The double-sided T-joint and double-sided cruciform joint are characteristic ones, e.g. connecting frames and bottom/side/deck plates or bulkheads (Figure 1). The marine structural stiffness distribution is predominantly orthotropic (stiffened panels) or member orientation defined (trusses and frames), meaning the uniaxial crack opening mode-I component dominates the welded joint fatigue damage process.

Different fatigue assessment concepts, relating the fatigue life time and a fatigue strength criterion using a resistance curve, have been developed over time aiming to obtain more accurate life time estimates, balanced with criterion complexity and (computational) efforts. The fatigue strength criteria have evolved from global to local ones and tend to become more generalised formulations, reducing the number of corresponding resistance curves accordingly. The nominal stress, hot spot structural stress and effective notch stress concepts are commonly applied in engineering. Several design guidelines (e.g. IIW), standards (e.g. EuroCode) and classification notes (e.g. DNV-GL) are available.[8-10] Recently, the total stress concept has been developed,[7,11] aiming to improve fatigue strength similarity with respect to weld notch stress distribution, weld notch stress intensity, weld notch affected micro-crack and far field dominated macro-crack growth as well as welded joint fatigue resistance. Complete and censored data have been used to establish one (family of damage tolerant engineering) joint fatigue resistance curve(s) for arc-welded joints in aluminium marine structures. The obtained standard deviation and strength scatter band index are relatively small in comparison with results obtained using other fatigue assessment concepts, providing an incentive to explore the performance for arc-welded joints in steel marine structures as well. However, the geometry and loading & response-dependent properties for each welded joint do not show the required estimates and trends.

Starting with double-sided T-joints and double-sided cruciform joints reflecting respectively non-symmetry and symmetry with respect to half the plate thickness, the involved weld notch stress (intensity) distribution formulations will be improved first. Particular attention will be paid to the weld load carrying stress component (Section 2). Double-sided T-joint and double-sided cruciform joint fatigue resistance data from literature will be used to investigate the total stress concept performance in comparison with the nominal stress concept hot spot structural stress concept and effective notch stress concept results. Last but not least, taking advantage of the weld notch stress distribution formulation, a potential effective notch stress concept performance increase will be examined (Section 3).

## 2 | WELD NOTCH STRESS (INTENSITY) DISTRIBUTIONS

To calculate the (cyclic) mechanical loading induced global marine structural response, a relatively coarse meshed shell/plate finite element (FE) model is typically sufficient to estimate the far-field stress.[12,13] The local weld geometry is not included, meaning that corresponding notch information is missing. However, the (linear) predominant mode-I fatigue damage related far-field stress distribution in each cross-section along the weld seam is available. The through-thickness weld toe and weld root notch stress distributions along the expected (2D) crack

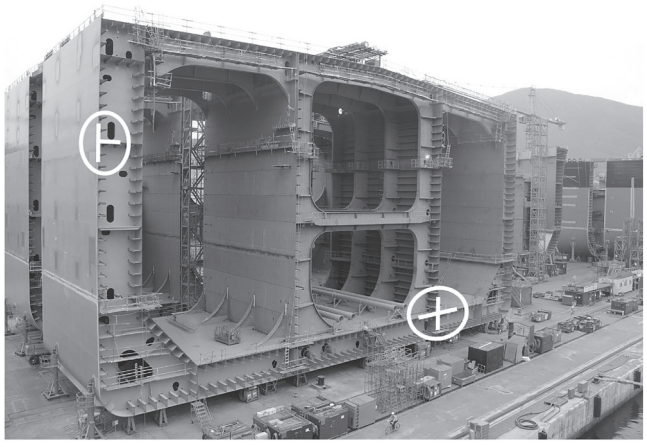

**FIGURE 1** Double-sided T-joints and double-sided cruciform joints in a marine (hull) structure

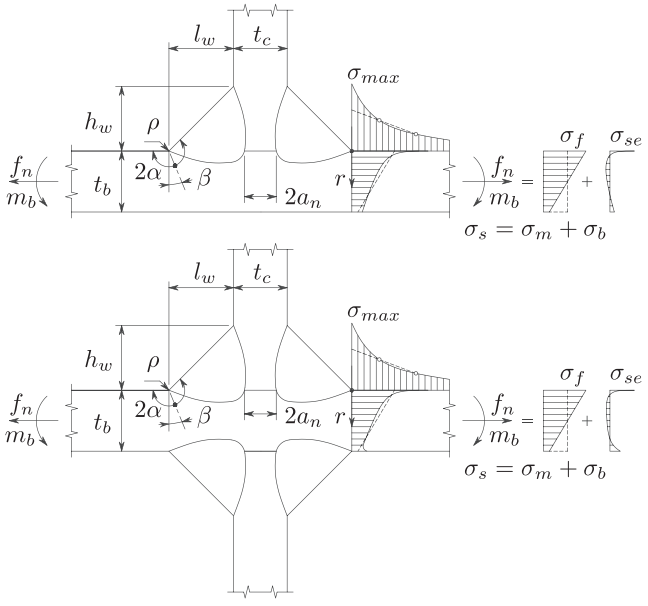


**FIGURE 2** Partially penetrated double-sided T-joint and double-sided cruciform weld toe notch stress distribution

path are assumed to be a key element in defining an appropriate fatigue design (and detectable repair) criterion. Exploiting (non-)symmetry conditions, a generalised semi-analytical formulation-related to the far-field stress distribution has been obtained, demonstrating stress field similarity and extends to the welding-induced thermal residual stress distribution. A linear superposition of the two distributions provides the total one. Since fatigue scaling requires both the peak value and gradient to be incorporated, the total weld notch stress distribution has been used to obtain the total weld notch stress intensity distribution. Turning an intact geometry parameter into a cracked geometry equivalent, the acquired damage criterion takes the complete distribution into account.[7,11]

## 2.1 | Weld notch stress distributions

The arc-welded double-sided T-joint is a characteristic one in marine structures, showing non-symmetry with respect to half the base plate thickness ($t_b/2$). The fillet weld geometries introduce notches at the weld toes and depending on penetration level at the weld roots as well; fatigue-sensitive locations of the hot spot type *C*. The geometry and loading & response conditions define the governing ones. Focus will be on base plate loaded T-joints (Figure 2), meaning the related weld toe notches are in charge.

Weld notch stress distribution $\sigma_n(r/t_p)$ is assumed to be a linear superposition of an equilibrium equivalent part $\sigma_f$ (i.e. the linear structural field stress) and a self-equilibrating stress part $\sigma_{se}$ (consisting of a V-shaped notch stress component and a weld load carrying stress component). For the non-symmetry case with $t_p = t_b$, the distribution denotes[7]:

$$\begin{aligned}\sigma_n\left(\frac{r}{t_p}\right) = \sigma_s \Bigg\{ &\left(\frac{r}{t_p}\right)^{\lambda_s-1} \mu_s\lambda_s\left(\lambda_s+1\right)\left[\cos\left\{\left(\lambda_s+1\right)\beta\right\}\right. \\ &\left. -\ \chi_s\cos\left\{\left(\lambda_s-1\right)\beta\right\}\right] \\ &+\left(\frac{r}{t_p}\right)^{\lambda_a-1} \mu_a\lambda_a\left(\lambda_a+1\right)\left[\sin\left\{\left(\lambda_a+1\right)\beta\right\}\right. \\ &\left. -\ \chi_a\sin\left\{\left(\lambda_a-1\right)\beta\right\}\right] \\ &+\ C_{bw}\cdot\left\{2\left(\frac{r}{t_p}\right)-1\right\}-2\cdot r_s\cdot\left(\frac{r}{t_p}\right)\Bigg\}\end{aligned} \tag{1}$$

with

$$\mu_s = \frac{C_{bw}\left(\lambda_a+1\right)+3\left(\lambda_a-1\right)}{6\left(\lambda_a-\lambda_s\right)\left[\cos\left\{\left(\lambda_s+1\right)\beta\right\}-\chi_s\cos\left\{\left(\lambda_s-1\right)\beta\right\}\right]}$$

$$\mu_a = \frac{C_{bw}\left(\lambda_s+1\right)+3\left(\lambda_s-1\right)}{6\left(\lambda_a-\lambda_s\right)\left[\sin\left\{\left(\lambda_a+1\right)\beta\right\}-\chi_a\sin\left\{\left(\lambda_a-1\right)\beta\right\}\right]}$$

and

$$\chi_s = \frac{\cos\left\{\left(\lambda_s+1\right)\alpha\right\}}{\cos\left\{\left(\lambda_s-1\right)\alpha\right\}}$$

$$\chi_a = \frac{\sin\left\{\left(\lambda_a+1\right)\alpha\right\}}{\sin\left\{\left(\lambda_a-1\right)\alpha\right\}}.$$

The symmetric as well as anti-symmetric V-shaped notch stress term $(r/t_p)^{\lambda_s-1}(\cdot)$ and $(r/t_p)^{\lambda_a-1}(\cdot)$ are incorporated,[14,15] reflecting the mixed mode-I/mode-II multi-axial notch stress state. Mode-III induced 3D effects have been neglected.[16] Notch radius $\rho = 0$, an artificial limit case introducing a singularity at $\sigma_n(r/t_p = 0)$. Weld load carrying stress $C_{bw}\left\{2(r/t_p)-1\right\}$ contains a linear bending term. The (unit) weld geometry stress distribution, $\sigma_{se}+1$, is scaled and projected onto the structural field stress distribution using respectively $\sigma_s = (\sigma_m+\sigma_b)$ and $r_s = (\sigma_b/\sigma_s)$. Coefficients $\mu_s$ and $\mu_a$ are obtained using force and moment equilibrium. The involved eigenvalues $\lambda_s$ and $\lambda_a$, the eigenvalue coefficients $\chi_s$ and $\chi_a$ and the stress angle $\beta = (\alpha - \pi/2)$ are notch angle $\alpha$ dependent.[7] Three zones can be identified for all weld notch stress distributions: the zone 1 peak stress value, the zone 2 notch-affected stress gradient and the zone 3 far-field dominated stress gradient, demonstrating stress field similarity.

Weld toe notches appear at both sides of the base plate if symmetry with respect to $(t_p/2)$ is detected, as shown for an arc-welded double-sided cruciform joint (Figure 2). The notch stress for the symmetry part will be ignored, assuming $\sigma_{se}$ is important for the considered notch only. For base plate loaded cruciform joints, the related weld toe notches are the governing fatigue sensitive locations of the hot spot type *C*. The $\sigma_n(r/t_p)$ distribution with $t_p = t_b$ yields[7]:

$$\begin{aligned}\sigma_n\left(\frac{r}{t_p}\right) = \sigma_s \Bigg\{ &\left[1-2\cdot r_s\cdot\left\{1-f\left(\frac{r}{t_p}=\frac{1}{2}\right)\right\}\right] f\left(\frac{r}{t_p}\right) \\ &+ r_s\cdot\left\{2\cdot f\left(\frac{r}{t_p}=\frac{1}{2}\right)-1\right\} \\ &\cdot\left[\left\{1-f\left(\frac{r}{t_p}=\frac{1}{2}\right)\right\}-2\cdot\left(\frac{r}{t_p}\right)\right]\Bigg\}\end{aligned} \tag{2}$$

with

$$\begin{aligned}f\left(\frac{r}{t_p}\right) = \sigma_s \Bigg\{ &\left(\frac{r}{t_p}\right)^{\lambda_s-1} \mu_s\lambda_s\left(\lambda_s+1\right)\left[\cos\left\{\left(\lambda_s+1\right)\beta\right\}\right. \\ &\left. -\ \chi_s\cos\left\{\left(\lambda_s-1\right)\beta\right\}\right] \\ &+\left(\frac{r}{t_p}\right)^{\lambda_a-1} \mu_a\lambda_a\left(\lambda_a+1\right)\left[\sin\left\{\left(\lambda_a+1\right)\beta\right\}\right. \\ &\left. -\ \chi_a\sin\left\{\left(\lambda_a-1\right)\beta\right\}\right] \\ &+\ C_{bw}\cdot\left\{4\left(\frac{r}{t_p}\right)-1\right\}-2\cdot r_s\cdot\left(\frac{r}{t_p}\right)\Bigg\}\end{aligned}$$

and

$$f\left(\frac{r}{t_p}=\frac{1}{2}\right)=\frac{(\lambda_a-\lambda_s)(\lambda_a\lambda_s-2C_{bw})}{\lambda_a(\lambda_a-1)-\lambda_s(\lambda_s-1)}+C_{bw}$$

and

$$\mu_s=\frac{\frac{1}{2}\lambda_a(\lambda_a-1)+C_{bw}}{C_s\left[\cos\{(\lambda_s+1)\beta\}-\chi_s\cos\{(\lambda_s-1)\beta\}\right]}$$
$$\mu_a=\frac{\frac{1}{2}\lambda_s(\lambda_s-1)+C_{bw}}{C_a\left[\cos\{(\lambda_a+1)\beta\}-\chi_a\cos\{(\lambda_a-1)\beta\}\right]}$$

and

$$C_s=\left(\frac{1}{2}\right)^{\lambda_s}(\lambda_s+1)\{\lambda_a(\lambda_a-1)-\lambda_s(\lambda_s-1)\}$$
$$C_a=\left(\frac{1}{2}\right)^{\lambda_a}(\lambda_a+1)\{\lambda_a(\lambda_a-1)-\lambda_s(\lambda_s-1)\}.$$

In comparison with $\sigma_n(r/t_p)$ for the non-symmetry case (Equation 1), the unit stress distribution for a normal force induced membrane stress component $f(r/t_p)$ is shifted and scaled to meet the bending moment induced bending stress component requirements. Note that the weld load carrying stress $C_{bw}\left\{4(r/t_p)-1\right\}$ has been modified in order to obtain a linear bending term over half the plate thickness.

### 2.1.1 | Weld load carrying stress component

The weld geometry causes a local change in stiffness, a shift in neutral axis, meaning the weld becomes load carrying up to some extent. Considering a weld toe notch as typically encountered in a double-sided T-joint at the base plate $t_b$ without symmetry, a counter-clockwise bending moment is introduced for a normal force $f_n$ pointing to the right and a clockwise bending moment $m_b$. The corresponding weld load carrying (bending) stress distribution particularly affects the zone 2 stress gradient (Equation 1). For a weld toe notch of a double-sided cruciform joint, the same principle applies to the related half plate thickness.

The weld load carrying stress component is geometry ($t_b$, $t_c$, $l_w$, $h_w$ and $a_n$) and loading ($f_n$ and $m_b$) dependent, meaning $C_{bw}$ contains the notch stress distribution specific information. With respect to loading, $\sigma_s C_{bw}$ is assumed to be linear superposition of a normal force and bending moment induced structural field membrane stress and bending stress component:

$$\sigma_s C_{bw}=\sigma_m C_{bm}+\sigma_b C_{bb}, \tag{3}$$

meaning

$$C_{bm}=\frac{m_{bm}}{\sigma_s(1-r_s)}\cdot\left(\frac{6}{t_p^2}\right)$$

and

$$C_{bb}=\frac{m_{bb}}{\sigma_s r_s}\cdot\left(\frac{6}{t_p^2}\right).$$

Bending moments $m_{bm}$ and $m_{bb}$ are estimated using an FE beam model in order to obtain weld load carrying stress information, uncoupled from V-shaped notch behaviour. Alternatively, a $C_{bw}$ estimate is obtained using a parametric function, fitted with input from FE notch stress distributions for a range of geometry dimensions and loading parameter values.

### 2.1.2 | Weld load carrying stress estimate

Originally, single weld element beam models (Figure 3 left) have been developed.[7,9] However, the model turned out not to be able to estimate the required $m_{bm}$ and $m_{bb}$ trends for the full range of geometry dimensions. Double weld element beam models (Figure 3, right) are proposed to improve the results, being able to deal with both base plate and cross plate loading at the same time. Because of the two parallel weld elements, each element contains half the throat size in order to prevent for an artificial stiffness increase.

As a first step in the double weld element beam model verification, the base plate loads $f_{n,t_b}$ and $m_{b,t_b}$ for respectively two load cases, a normal force $f_n$ and bending moment $m_b$, have been compared with results obtained using the single weld element beam model as well as a FE solid model for reference (Figures 4 and 5). The considered range of joint dimensions is representative for marine structures consisting of thin plate/shell structural members.

In case loading is applied to the base plate, the double sided T-joint contains two parallel load paths: one through the base plate and one through the weld and cross plate. The normal stiffness and bending stiffness of the load paths define how the loading is divided. For an applied normal force $f_n$, the base plate load path related normal stiffness dominates the weld and cross plate load path related bending stiffness, explaining the values close to 1 (Figure 4A-D). The bending stiffness is involved for both load paths if a bending moment $m_b$ is applied, clarifying the more balanced distribution of the load over the two paths (Figure 5A-D); i.e. the weld is relatively more load carrying. For the double-sided cruciform joint, three parallel load paths are involved: one through the base plate and two through the weld and cross plate, meaning the normal forces (Figure 4E-H) and bending moments (Figure 5E-H) through the base plate will be smaller in comparison with the double-sided T-joint values (Figure 4A-D and Figure 5A-D) because of the relatively smaller stiffness contribution of each load path. The double-weld element beam models show improved behaviour in comparison

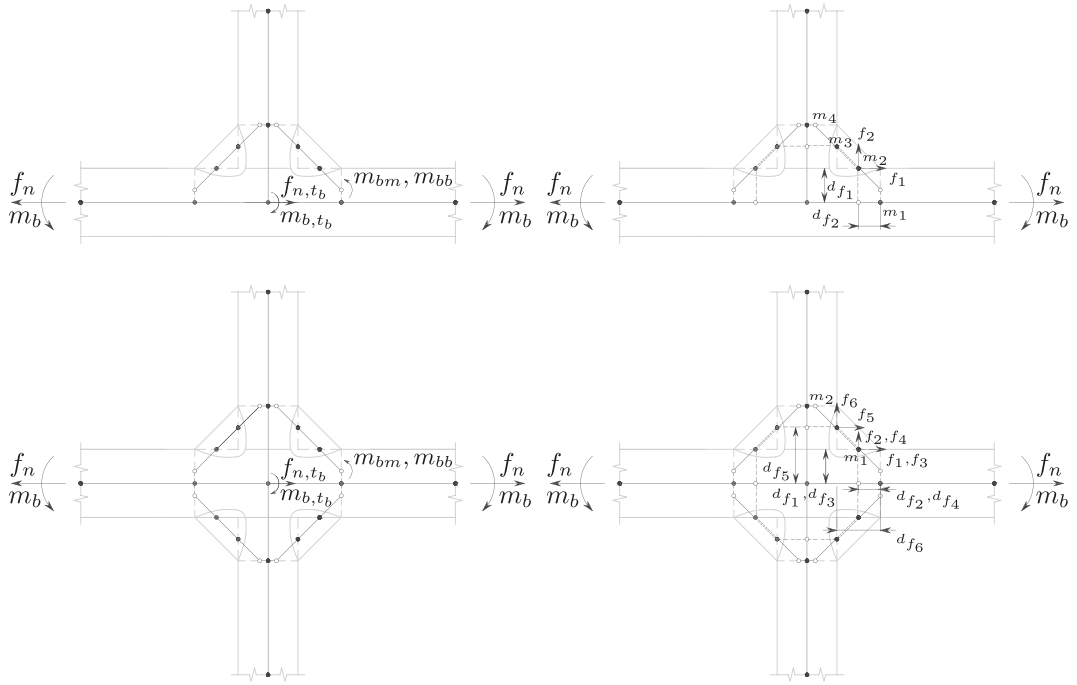


**FIGURE 3** Single weld element beam model (left) and double weld element beam model (right)

with the single-weld element beam models with respect to the solid model reference values. The trends for $f_n$ and $m_b$ are the same. For increasing $t_b$, the normal force and bending moment through the base plate are increasing because of increasing base plate load path stiffness. The weld and cross plate load path bending stiffness is increasing for increasing $t_c$, $l_w$, and $h_w$, meaning the base plate load path contribution is decreasing. For $h_w$ variations (Figures 4 and 5), the wrong trend for the single-weld element beam models can be observed.

Second step is to correlate the beam model nodal moments and forces to $m_{bm}$ and $m_{bb}$ (Equation 3). For the $f_n$ load case, internal bending moments are introduced, and the ones showing the same trend as the required $C_{bm}$ (obtained fitting FE solid model weld notch stress distributions and the semi-analytical formulation, Equations 1 and 2) for varying joint dimensions, $m_1$ to $m_4$ (Figure 3), can be related to $m_{bm}$. Assuming that except $m_1$ to $m_4$ in the weld toe cross-section (the physical part), a coefficient to match the FE and semi-analytical solutions (the fitting part) is involved as well, the $m_{bm}$ estimate yields for the double-sided T-joint:

$$m_{bm} = \left(\frac{1}{2}\right) \cdot (m_1 + m_2 + m_3 + m_4). \tag{4}$$

For the $m_b$ load case, internal normal forces are introduced and $f_1$ and $f_2$ (Figure 3) show the same trend as the required $C_{bb}$. Involving respectively $d_{f_1}$ and $d_{f_2}$ to complete the physical part related bending moment and adding the fitting part, the $m_{bb}$ estimate becomes for the double-sided T-joint:

$$m_{bb} = \left(\frac{3}{5}\right) \cdot \left(f_1 \cdot d_{f_1} + f_2 \cdot d_{f_2}\right). \tag{5}$$

For the double-sided cruciform joint, similar results are obtained:

$$m_{bm} = m_1 + m_2 \tag{6}$$

and

$$\begin{aligned} m_{bb} = \left(\frac{1}{18}\right) \cdot \{ & \left(f_1 \cdot d_{f_1} + f_2 \cdot d_{f_2}\right) \\ & + \left(f_3 \cdot d_{f_3} + f_4 \cdot d_{f_4}\right) \\ & - \left(f_5 \cdot d_{f_5} + f_6 \cdot d_{f_6}\right) \}. \end{aligned} \tag{7}$$

Comparing for the double-sided T-joint the required $C_{bm}$ and $C_{bb}$ values with the estimates (Figure 6), good results are obtained. Depending on the joint dimensions, the weld load carrying stress level for the base plate weld toe notch can be up to 30% of the structural stress $\sigma_s$. On the other hand, for double-sided cruciform joints, the weld load carrying stress level does not even reach 10% of $\sigma_s$ (Figure 6).

For varying $t_b$, $t_c$, and $h_w$, the trends (Figure 6) are the same and opposite to the relative base plate loads (Figures 4 and 5) as expected because of the same physics. Increasing $t_b$ decreases $C_{bm}$ and $C_{bb}$ since the relative stiffness contribution of the weld and cross plate load path decreases. For increasing $t_c$ and $h_w$, the $C_{bm}$ and $C_{bb}$ values increase because the relative weld and cross plate load path stiffness increases. For increasing $l_w$, the load through the base plate decreases for both the T-joint and the cruciform joint (Figures 4 and 5); the load through the weld (throat) and cross plate increases accordingly. However, the T-joint $C_{bm}$ decreases for increasing $l_w$ (Figure 6), meaning the weld notch becomes less effective. The weld toe notch

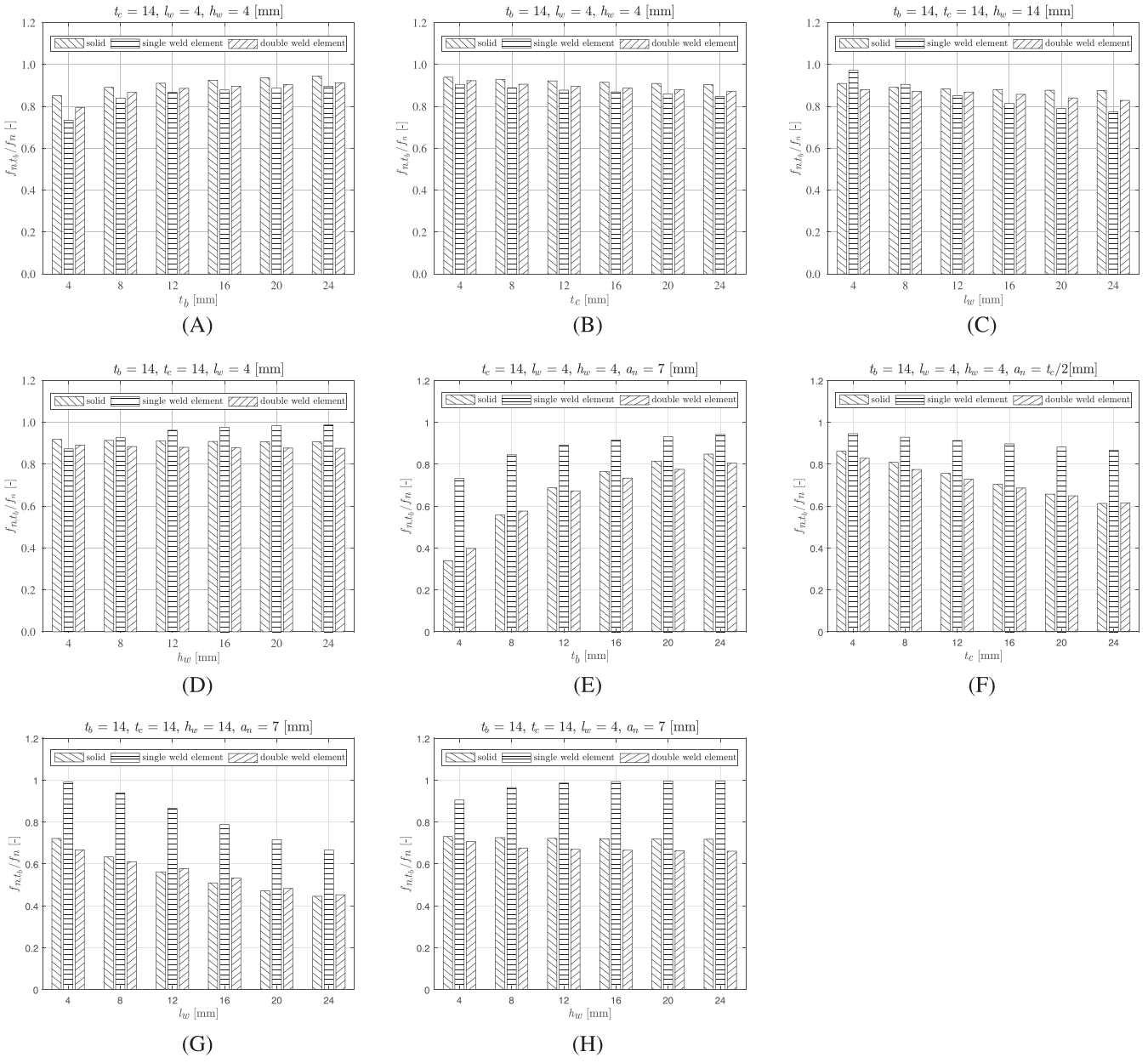


**FIGURE 4** Double-sided T-joint (A-D) and double-sided cruciform joint (E-H) relative base plate load for varying $t_b$, $t_c$, $l_w$ and $h_w$ and applied normal force

load carrying level hardly changes for increasing $l_w$ of the cruciform joint.

Alternative to a beam model-based weld load carrying stress estimate involving a physical and fitting part, a parametric fitting function has been obtained as well. For the double sided T joint:

$$\begin{aligned} C_{bm} &= 0.117 - 0.192 \cdot e^{-0.494 \cdot W} \\ &\quad + \frac{0.793 \cdot P^3 + 1.113 \cdot P^2 + 0.957 \cdot P + 0.9}{P^4 + 4.721 \cdot P^3 + 13 \cdot P^2 + 9.669 \cdot P + 9.079} \\ C_{bb} &= 0.123 - 0.261 \cdot e^{-0.712 \cdot W} \\ &\quad + \frac{0.143 \cdot P^4 + 1.007 \cdot P^3 + 1.438 \cdot P^2 + 1.674 \cdot P + 1.578}{P^4 + 3.892 \cdot P^3 + 9.41 \cdot P^2 + 7.57 \cdot P + 8.118}, \end{aligned} \tag{8}$$

and for the double sided cruciform joint:

$$\begin{aligned} C_{bm} &= 0.015 - 0.026 \cdot e^{-0.588 \cdot W} \\ &\quad + \frac{0.297 \cdot P + 0.22}{P^2 + 3.144 \cdot P + 4.478} \\ C_{bb} &= 0.028 - 0.039 \cdot e^{-0.340 \cdot W} \\ &\quad + \frac{0.044 \cdot P^2 + 0.141 \cdot P + 0.116}{P^2 + 2.881 \cdot P + 2.505} \end{aligned} \tag{9}$$

with

$$W = \left( \frac{h_w}{l_w} \right)$$

$$P = \log \left( \frac{t_c/2 + l_w}{t_b} \right).$$

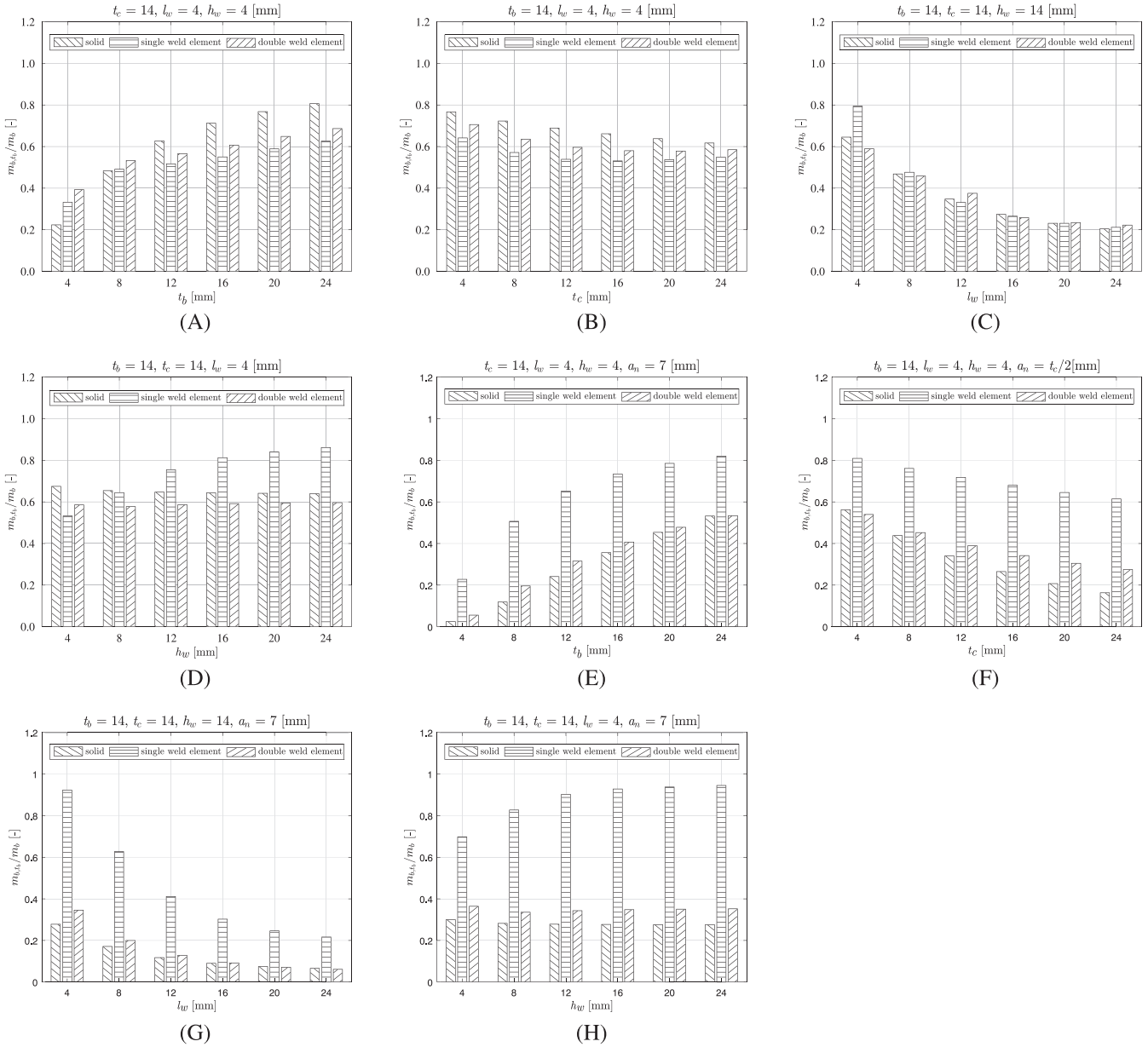


**FIGURE 5** Double-sided T-joint (A-D) and double-sided cruciform joint (E-H) relative base plate load for varying $t_b$, $t_c$, $l_w$ and $h_w$ and applied bending moment

The parametric fitting functions involve an exponential term reflecting a notch angle contribution as well as a polynomial one representing the log-ratio of the two involved load path parameters.

### 2.1.3 | Semi-analytical formulations, approximations and FE results

Third and last step is to investigate the weld toe notch stress distributions for different loading combinations. For illustration purposes, monotonic through-thickness weld toe notch stress distributions of a double-sided T-joint are shown (Figure 7A,B) for a pure bending moment ($r_s = 1$) and combined load case ($r_s = 1/3$); the bending moment is applied clockwise. Non-monotonic ones are shown for a pure normal force ($r_s = 0$) and a different combined load case ($r_s = -1$) with counter-clockwise bending moment (Figure 7C,D). The adopted joint dimensions are arbitrary but reflect at the same time results for cases with almost the largest difference between $C_{bw}$ fit and beam values (Figure 6).

Monotonic through-thickness weld toe notch stress distributions $\sigma_n(r/t_p)$ of a double-sided cruciform joint for the far-field load cases ($r_s = 1$) and ($r_s = 1/3$) are shown (Figure 7E and 7F) as well as non-monotonic ones (Figure 7G and 7H); ($r_s = 0$) and ($r_s = -1$). For $0 < (r/t_p) < (1/2)$ equilibrium is satisfied as imposed. The self-equilibrating stress part definition is lost for $(1/2) < (r/t_p) < 1$ since the weld notch contribution is not taken into account. The (anti-)symmetry condition ensures a

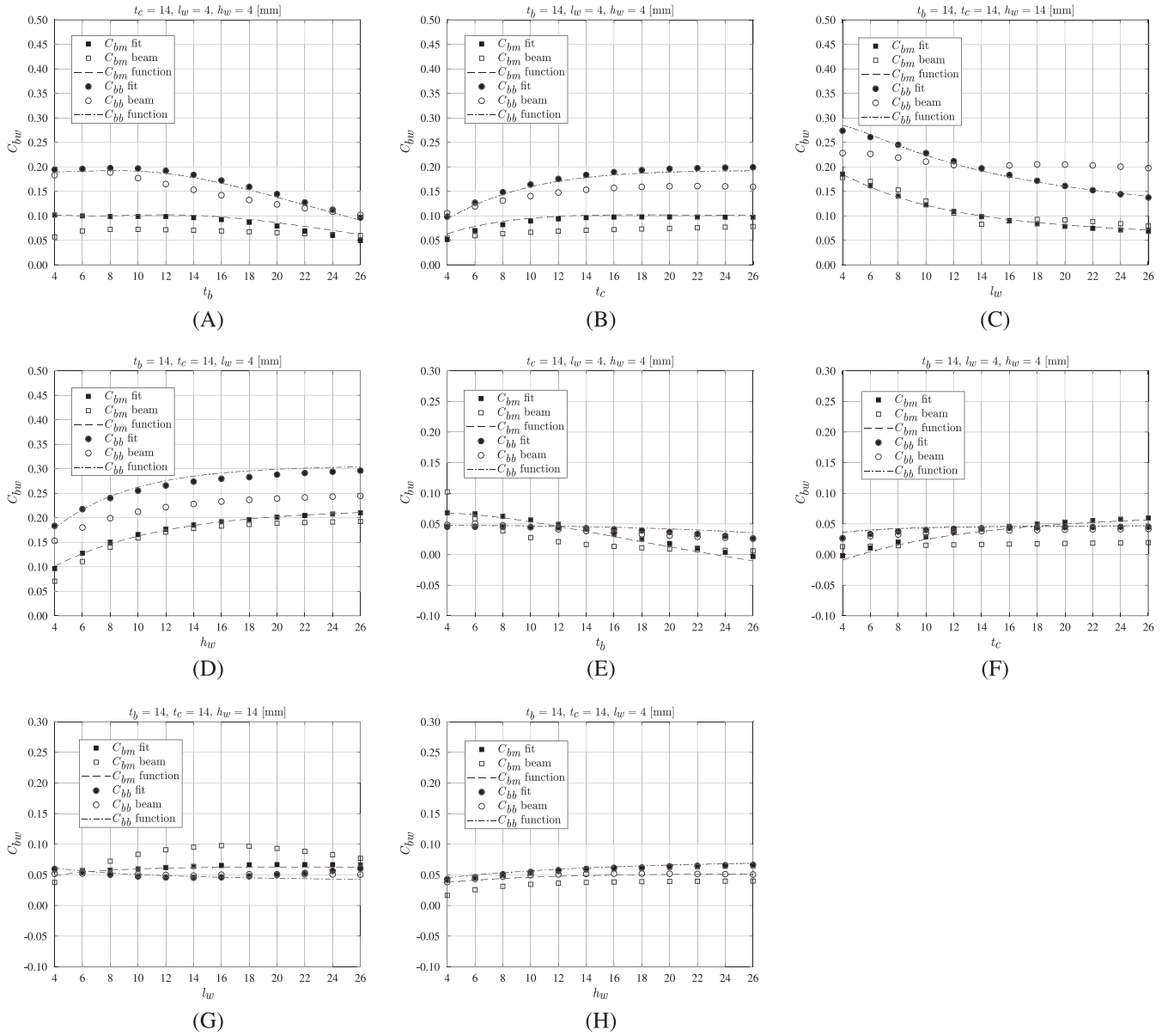


**FIGURE 6** Double-sided T-joint (A-D) and double-sided cruciform joint (E-H) $C_{bm}$ and $C_{bb}$ fit as well as beam model estimate for varying $t_b$, $t_c$, $l_w$, and $h_w$

stress gradient close to $r_s$. Converged FE solid model solutions are added for comparison, showing that the semi-analytical $\sigma_n(r/t_b)$ formulations (Equations 1 and 2) provide accurate weld toe notch stress distributions. The FE solid model solutions have been obtained using Ansys, involving linear elements in plane strain condition. Element size is $(t_b/40)$. Half the joint has been modelled taking advantage of symmetry with respect to $(t_c/2)$.

## 2.2 | Weld notch stress intensity distributions

Fatigue scaling requires both the (zone 1) peak stress value, the (zone 2) notch affected stress gradient and (zone 3) far-field dominated stress gradient to be taken into account, meaning a damage criterion should incorporate the total distribution. The stress intensity factor $K$, a first-order damage tolerant parameter, seems to meet this criterion, though, the intact geometry related notch stress distributions have to be turned into cracked equivalents; fatigue of welded joints is assumed to be a crack growth-dominated process. Consistently using the equilibrium equivalent and self-equilibrating parts of the intact geometry related mode-I weld toe notch stress distribution $\sigma_n$ (Equations 1 and 2), $K_I$ includes a crack size-dependent far field and notch factor[7]:

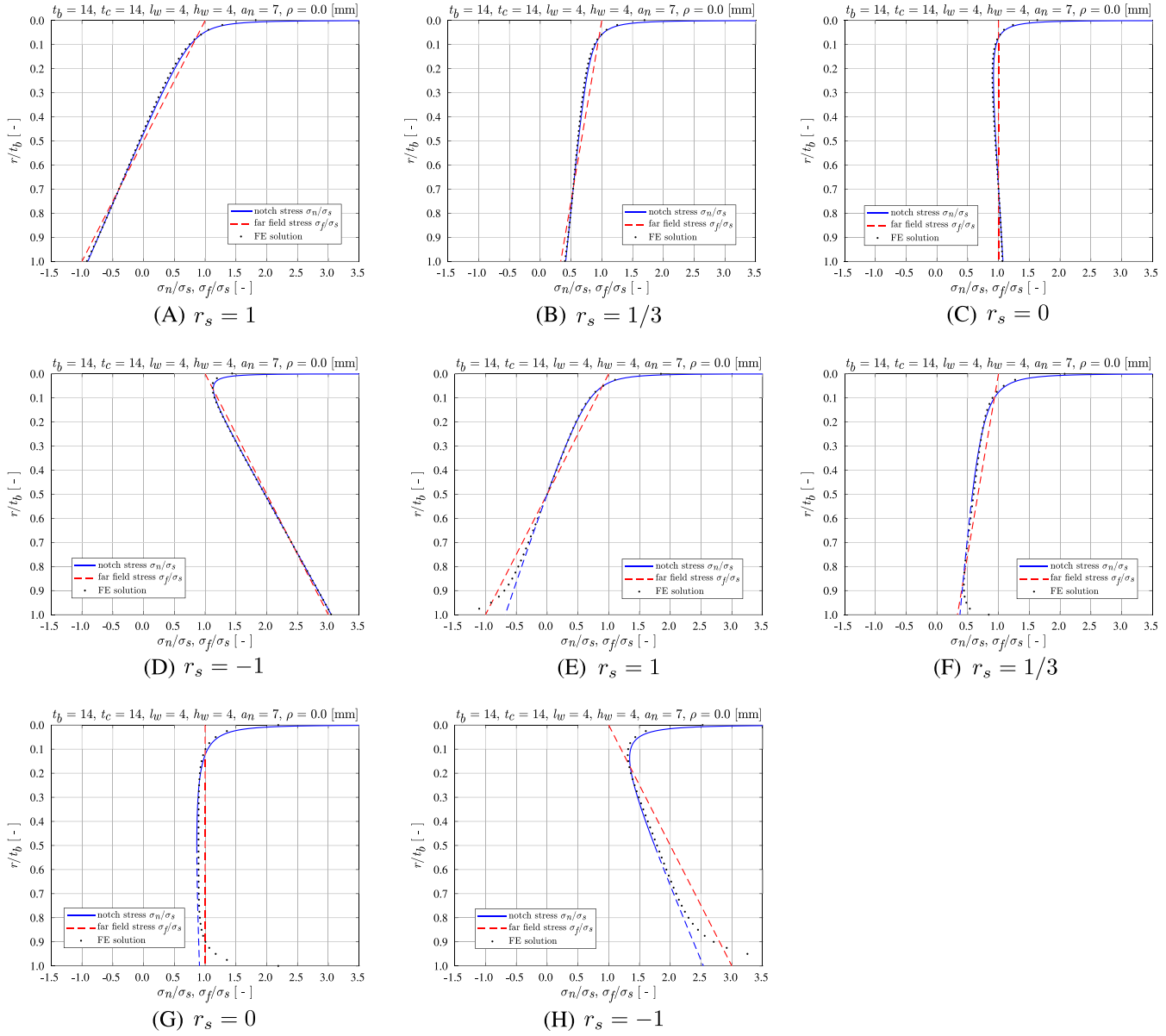


**FIGURE 7** Double-sided T-joint (A-D) and double-sided cruciform joint (E-H) base plate weld toe notch stress distributions [Colour figure can be viewed at wileyonlinelibrary.com]

$$K_I = \sigma_s \sqrt{t_p} \cdot Y_n\left(\frac{a}{t_p}\right) \cdot Y_f\left(\frac{a}{t_p}\right) \cdot \sqrt{\pi \cdot \left(\frac{a}{t_p}\right)}. \tag{10}$$

Far-field factor $Y_f$ contains the zone 3 associated equilibrium equivalent stress contributions (membrane and bending component) as well as the crack related geometry effects (finite plane dimensions and free surface behaviour). For a base plate related weld toe notch of the double-sided T-joint and cruciform joint, a single-edge crack formulaton is required. Handbook solutions[17] are available. Notch factor $Y_n$ incorporates the zones 1 and 2 governing self-equilibrium equivalent stress contribution, applied as crack face traction. For the double-sided T-joint[7]:

$$\begin{aligned} Y_n\left(\frac{a}{t_p}\right) = \left(\frac{2}{\pi}\right) \Bigg[ & \left(\frac{a}{t_p}\right)^{\lambda_s - 1} \mu_s \left(\frac{\sqrt{\pi}}{2}\right) \frac{\Gamma\left(\frac{\lambda_s}{2}\right)}{\Gamma\left(\frac{\lambda_s+1}{2}\right)} \lambda_s (\lambda_s + 1) \cdot \\ & \left[\cos\{(\lambda_s + 1)\beta\} - \chi_s \cos\{(\lambda_s - 1)\beta\}\right] \\ & + \left(\frac{a}{t_p}\right)^{\lambda_a - 1} \mu_a \left(\frac{\sqrt{\pi}}{2}\right) \frac{\Gamma\left(\frac{\lambda_a}{2}\right)}{\Gamma\left(\frac{\lambda_a+1}{2}\right)} \lambda_a (\lambda_a + 1) \cdot \\ & \left[\sin\{(\lambda_a + 1)\beta\} - \chi_a \sin\{(\lambda_a - 1)\beta\}\right] \\ & + C_{bw} \left\{ 2\left(\frac{a}{t_p}\right) - \frac{\pi}{2} \right\} \Bigg], \end{aligned} \tag{11}$$

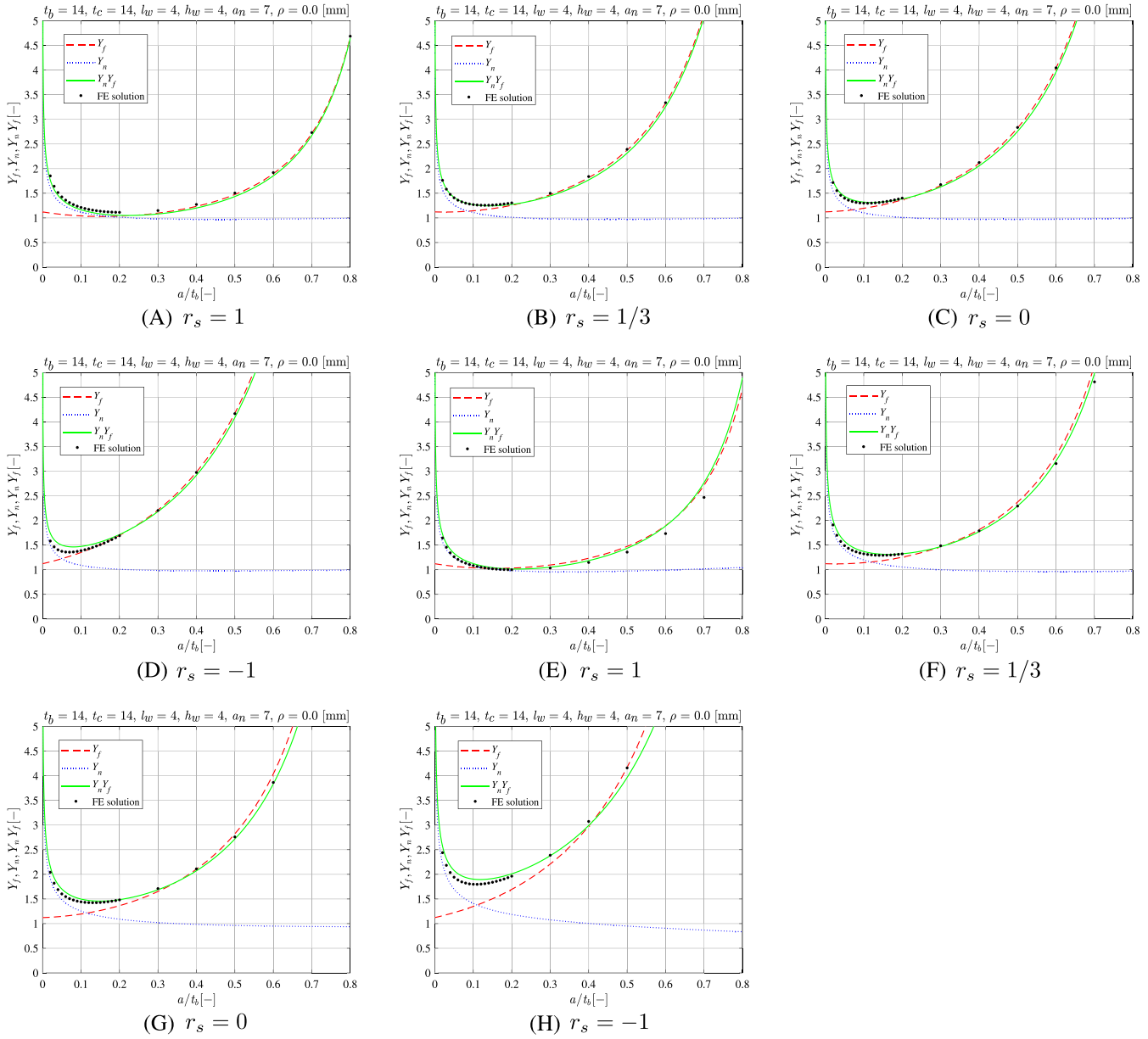


**FIGURE 8** Double-sided T-joint (A-D) and double-sided cruciform joint (E-H) base plate weld toe notch stress intensity distributions [Colour figure can be viewed at wileyonlinelibrary.com]

and for the double sided cruciform joint[7]:

$$
\begin{aligned}
Y_n\left(\frac{a}{t_p}\right) = \left(\frac{2}{\pi}\right)\Bigg(&\left[1-2r_s\left\{1-f\left(\frac{a}{t_p}=\frac{1}{2}\right)\right\}\right] f\left(\frac{a}{t_p}\right) \\
&+ r_s\left\{2f\left(\frac{a}{t_p}=\frac{1}{2}\right)-1\right\} \\
&\times\left[\left\{1-f\left(\frac{a}{t_p}=\frac{1}{2}\right)\right\}\left(\frac{\pi}{2}\right)-2\left(\frac{a}{t_p}\right)\right] \\
&+2r_s\left(\frac{a}{t_p}\right)\Bigg)
\end{aligned}
\tag{12}
$$

with

$$
\begin{aligned}
f\left(\frac{a}{t_p}\right) = &\left(\frac{a}{t_p}\right)^{\lambda_s-1}\mu_s\left(\frac{\sqrt{\pi}}{2}\right)\frac{\Gamma\left(\frac{\lambda_s}{2}\right)}{\Gamma\left(\frac{\lambda_s+1}{2}\right)}\lambda_s\left(\lambda_s+1\right) \\
&\left[\cos\left\{\left(\lambda_s+1\right)\beta\right\}-\chi_s\cos\left\{\left(\lambda_s-1\right)\beta\right\}\right] \\
&+\left(\frac{a}{t_p}\right)^{\lambda_a-1}\mu_a\left(\frac{\sqrt{\pi}}{2}\right)\frac{\Gamma\left(\frac{\lambda_a}{2}\right)}{\Gamma\left(\frac{\lambda_a+1}{2}\right)}\lambda_a\left(\lambda_a+1\right)\cdot \\
&\left[\sin\left\{\left(\lambda_a+1\right)\beta\right\}-\chi_a\sin\left\{\left(\lambda_a-1\right)\beta\right\}\right] \\
&+C_{bw}\left\{4\left(\frac{a}{t_p}\right)-\frac{\pi}{2}\right\}.
\end{aligned}
$$

With respect to $\sigma_n$ (Equations 1 and 2) through-thickness crack coordinate $(a/t_p)$ naturally replaced the through-thickness stress coordinate $(r/t_p)$. The weld toe notch stress intensities $Y_nY_f$ for the far-field load cases (Figure 7) are shown for illustration purposes (Figure 8). Notch factor $Y_n$ turns out to be governing for $\{0 < (a/t_p) \leq 0.2\}$; a zone 1 and 2 weld geometry stress (concentration) affected micro-crack region. Far-field factor $Y_f$ rules the zone 3 far-field stress related macro-crack region $\{0.2 < (a/t_p) \leq 1\}$. The $Y_nY_f$ estimates are in good agreement with FE solid model solutions. Note that the involved $C_{bw}$ values contain almost the largest difference between fit and beam values (Figures 6 and 7).

## 3 | FATIGUE RESISTANCE

Multiple arc-welded steel double-sided T-joint and double-sided cruciform joint constant amplitude resistance data series available in literature (Tables 1 and 2) have been reinvestigated. All small-scale specimens are in as-welded condition and failures have been obtained at the weld toe. The base plate thickness $t_b$ ranges from 5 to 160 mm, specimen width $w$ from 20 to 380 mm, the loading & response ratio $r_{rl}$ from –1.0 to 0.8 and the yield strength $S_y$ from 260 to 960 MPa. The applied load is either a (3 or 4 points) bending moment or a normal force. Fatigue life times $N$ cover the medium- and high-cycle fatigue (MCF and HCF) region; i.e. $N$ is in the range $10^4$ to $10^9$. For now, only complete (MCF failure) data are taken into account; censored (HCF run-out) data are ignored at the same time. For MCF and HCF, the far-field structural response is predominantly elastic, explaining why typical fatigue strength criteria $S$ are of the stress type. Involving the stress range $S = \Delta\sigma$ reflects the cyclic loading and response requirement to develop fatigue damage.[11]

Correlating a fatigue damage criterion $S$ to the fatigue life time $N$ for MCF resistance data, typically a(n approximately) log-log linear dependency is observed, and a Basquin type of relation is naturally adopted: $\log(N) = \log(C) - m\cdot \log(S)$. One way to estimate the single slope curve parameters, intercept $\log(C)$ and slope $m$ as respectively the endurance and damage mechanism coefficient, is using linear regression on fatigue life time: $\log(N) = \log(C) - m\cdot \log(S) + \sigma\varepsilon$. The Maximum Likelihood approach[7,42] will be employed to obtain the parameter estimates.

To investigate the performance of respectively the nominal stress concept, hot spot structural stress concept, effective notch stress concept, and total stress concept, the standard deviation $\sigma$ and strength scatter band index $T_{\sigma S} = 1 : (S_{10}/S_{90})$, the fatigue strength ratio for 10% and 90% probability of survival, will be evaluated.

### 3.1 | Nominal stress concept

The nominal stress criterion $S_n$ is a global structural detail reference- and linear elastic intact geometry parameter. Constant amplitude fatigue resistance information is typically expressed in terms of FATigue classes, defining the intercept $\log(C)$. The damage process is assumed to be similar for all structural details, meaning the slope $m$ is invariant. The IIW has assigned FAT80 for steel as-welded double-sided T-joint fatigue resistance in air with $t_b \leq t_c$, meaning $S_n = 80$ MPa at $N = 2{\cdot}10^6$ cycles. Failure is base plate weld toe induced, and angular misalignments up to 20% of $S_n$ are already included. The $S_n$ values of the considered fatigue resistance data subjected to a normal force have been modified accordingly and include a bending stress component $0.2S_n$ in order to meet the FAT class requirements. For double-sided cruciform joints, the same FAT class is adopted. However, because of symmetry with respect to $(t_p/2)$, no angular misalignment is incorporated. Normal force and bending moment induced differences in far-field stress distribution are not distinguished. Dimensional variations are not explicitly considered, paying off in terms of fatigue resistance accuracy (i.e. life time estimate uncertainty) since $S_n$ is processed as point criterion, as "local" nominal stress, meaning notch stress gradient induced size effects are not taken into account explicitly and have to be corrected for. Since the IIW FAT class prescriptions have been obtained considering structural details with $t_b \leq 25$ mm, only for $t_b > 25$ mm, an effective $S_n$ value is required (Equation 13).[8] The involved exponent is basically the zone 2 stress gradient; i.e. $\sim (\lambda_s - 1)$.

$$S_{n,eff} = S_n \cdot \left(\frac{t_{eff}}{t_{ref}}\right)^k \text{for} t_b > 25\text{mm} \tag{13}$$

with

$$\begin{aligned} t_{ref} &= 25 \\ k &= 0.3 && \text{for T-Joints and cruciform joints} \\ t_{eff} &= t_b && \text{for } \frac{t_c + 2\cdot l_w}{t_b} > 2 \\ t_{eff} &= \max\left(t_b, \frac{t_c + 2\cdot l_w}{2}\right) && \text{for } \frac{t_c + 2\cdot l_w}{t_b} \leq 2. \end{aligned}$$

Although a spatial description of a mechanical loading and structural response requires two parameters, e.g. range and ratio $r_{lr} = F_{min}/F_{max} = \sigma_{min}/\sigma_{max}$, the ratio is not explicitly considered since the stress level in the notch affected region is assumed to be at yield magnitude because of the welding induced residual stress. Any small- and large-scale specimen fatigue test result obtained at relatively low ratio has been translated to $r_{lr} \sim 0.5$ using a nominal mean stress correction.[11] Exponential mean stress models have been developed in order to improve the life time estimates in case of relatively low stress range and high mean

**TABLE 1** Double-sided T-joint fatigue resistance data

| group | reference | *loading*[a] | $t_b$ mm | $t_c$ mm | $l_w$ mm | $h_w$ mm | $a_n$ mm | $w$ mm | $r_{lr}$ - | $S_y$ MPa |
|---|---|---|---|---|---|---|---|---|---|---|
| 1 | [18] | 3B | 9 | 16 | 6 | 6 | 0 | 50 | 0.1 | 600 |
| 2 | [18] | 3B | 15 | 16 | 6 | 6 | 0 | 50 | 0.1 | 590 |
| 3 | [19] | 3B | 22 | 10 | 9 | 9 | 5 | 100 | 0.1 | 443 |
| 4 | [19] | 3B | 22 | 22 | 16 | 16 | 11 | 100 | 0.1 | 443 |
| 5 | [18] | 3B | 24 | 16 | 6 | 6 | 0 | 65 | 0.1 | 630 |
| 6 | [18] | 3B | 34 | 16 | 6 | 6 | 0 | 90 | 0.1 | 590 |
| 7 | [19] | 3B | 40 | 22 | 16 | 16 | 11 | 100 | 0.1 | 430 |
| 8 | [18] | 3B | 50 | 16 | 6 | 6 | 0 | 130 | 0.1 | 520 |
| 9 | [18] | 3B | 50 | 50 | 19 | 19 | 0 | 130 | 0.1 | 520 |
| 10 | [19] | 3B | 80 | 22 | 16 | 16 | 11 | 100 | 0.1 | 420 |
| 11 | [19] | 3B | 80 | 40 | 32 | 32 | 20 | 100 | 0.1 | 420 |
| 12 | [20] | 4B | 5 | 5 | 7 | 7 | 1 | | 0.1 | 700 |
| 13 | [20] | 4B | 6 | 6 | 6 | 6 | 3 | | 0.1 | 355 |
| 14 | [21] | 4B | 6 | 6 | 6 | 6 | 3 | 50 | 0.1 | 700 |
| 15 | [22] | 4B | 8 | 8 | 7 | 7 | 4 | 40 | 0.1 | 960 |
| 16 | [23] | 4B | 15 | 15 | 6 | 9 | 0 | 100 | 0.1 | 700 |
| | [23] | 4B | 15 | 15 | 6 | 9 | 0 | 100 | 0.5 | 700 |
| 17 | [24] | 4B | 16 | 8 | 7 | 7 | 2 | 100 | 0.5 | 550 |
| | [24] | 4B | 16 | 8 | 7 | 7 | 2 | 100 | 0.0 | 550 |
| | [24] | 4B | 16 | 8 | 7 | 7 | 2 | 100 | 0.5 | 690 |
| | [24] | 4B | 16 | 8 | 7 | 7 | 2 | 100 | 0.0 | 690 |
| 18 | [25] | 4B | 20 | 20 | 21 | 21 | 5 | 50 | 0.1 | 420 |
| 19 | [26] | 4B | 20 | 20 | 21 | 21 | 5 | 50 | 0.1 | 420 |
| 20 | [27] | 4B | 40 | 20 | 11 | 18 | 0 | 210 | 0.1 | 432 |
| 21 | [27] | 4B | 70 | 35 | 10 | 19 | 0 | 210 | 0.1 | 429 |
| 22 | [28] | N | 5 | 5 | 6 | 6 | 4 | 50 | 0.1 | 960 |
| 23 | [29] | N | 5 | 5 | 6 | 6 | 2 | 50 | 0.1 | 355 |
| | [29] | N | 5 | 5 | 6 | 6 | 2 | 50 | 0.1 | 690 |
| | [29] | N | 5 | 5 | 6 | 6 | 2 | 50 | 0.1 | 960 |
| 24 | [22] | N | 8 | 8 | 7 | 7 | 4 | 40 | 0.3 | 960 |

[a] 3B, three point bending; 4B, four point bending; N, normal force

stress, e.g. welded joints operating in the MCF and HCF region. Walker's mean stress model is an important one (Equation 14).[7,43] The loading & response ratio coefficient $\gamma$ is a fitting parameter. In order to translate $r_{lr}$ for the fatigue resistance data to the IIW FAT class value, the effective stress becomes:

$$S_{n,eff} = S_n \cdot \frac{(1-0.5)^{1-\gamma}}{(1-r_{rl})^{1-\gamma}}. \tag{14}$$

Applying regression analysis to the nominal stress-based MCF resistance data without size and loading & response ratio corrections (Equations 13 and 14) for reference provides $\sigma = 0.33$ and $T_{\sigma S} = 1{:}2.46$ (Figure 9). A logNormal life time distribution is adopted as it provides a better fit than the (typically HCF related) extreme Weibull distribution. Of the approximately 600 considered data points (around 300 for each type of joint), 7 data points providing a significant longer fatigue life time are considered as outliers and have been ignored. The 95% point wise lower and upper confidence bounds (LCB and UCB) for respectively the 1% and 99% reliability levels show an approximately constant interval over the full MCF region. Looking at the slope reflected in the confidence bounds and the data, intuitively a larger value might be expected. However, an intuitive slope is typically related to regression based on fatigue strength rather than fatigue life time.

In order to estimate the resistance curve parameters intercept log($C$) and slope $m$ and to establish a design curve with 99% reliability and 95% confidence, size and loading & response ratio corrections (Equations 13 and 14) are incorporated (Figure 10A). In comparison with the IIW FAT80 curve parameter values, differences can be observed. Slope $m$ is different from the commonly adopted value of 3. Since $\gamma$ is close to 1, the stress range dominates the fatigue damage process and the maximum or mean stress hardly contributes. The performance parameters $\sigma = 0.32$ and $T_{\sigma S} = 1{:}3.19$ are larger than typical values: respectively 0.25 and 1:1.5.

The influence of size, i.e. base plate thickness $t_b$, may not be fully incorporated since for larger $t_b$ values, the data are at the lower bound of the data scatter band (Figure 10B). For loading & response ratio $r_{lr}$, the distribution seems reasonable (Figure 10C), although the $r_{lr} = 0.0$ data set is at the data scatter band lower bound. The

**TABLE 2** Double-sided cruciform joint fatigue resistance data

| group | reference | *loading*[a] | $t_b$ mm | $t_c$ mm | $l_w$ mm | $h_w$ mm | $a_n$ mm | $w$ mm | $r_{lr}$ - | $S_y$ MPa |
|---|---|---|---|---|---|---|---|---|---|---|
| 25 | [30] | N | 6 | 6 | 3 | 3 | 0 | 95 | −1.0 | 632 |
| 26 | [31] | N | 6 | 6 | 7 | 7 | 3 | | 0.1-0.6 | 355 |
| | [31] | N | 6 | 6 | 7 | 7 | 3 | | 0.1-0.8 | 650 |
| | [31] | N | 6 | 6 | 7 | 7 | 3 | | 0.1-0.8 | 960 |
| 27 | [32] | N | 9 | 9 | 5 | 5 | 4 | 40 | 0.0 | 523 |
| 28 | [19] | N | 10 | 5 | 4 | 4 | 2 | 80 | 0.0 | 430 |
| 29 | [19] | N | 10 | 10 | 9 | 9 | 5 | 80 | 0.0 | 430 |
| 30 | [19] | N | 10 | 22 | 16 | 16 | 11 | 80 | 0.0 | 430 |
| 31 | [30] | N | 11 | 11 | 5 | 5 | 5 | 95 | −1.0 | 671 |
| 32 | [33] | N | 12 | 12 | 6 | 6 | 6 | 40 | 0.1 | 355 |
| | [33] | N | 12 | 12 | 6 | 6 | 6 | 40 | 0.1 | 460 |
| | [33] | N | 12 | 12 | 6 | 6 | 6 | 40 | 0.1 | 690 |
| 33 | [34] | N | 12 | 12 | 8 | 8 | 6 | 84 | 0.1 | 550 |
| 34 | [35] | N | 13 | 10 | 8 | 8 | 5 | 201 | 0.0 | 398 |
| 35 | [30] | N | 19 | 19 | 8 | 8 | 9 | 95 | −1.0 | 616 |
| 36 | [36] | N | 20 | 20 | 10 | 10 | 10 | 40 | 0.0 | 654 |
| 37 | [37] | N | 20 | 20 | 10 | 10 | 10 | 40 | 0.0 | 538 |
| 38 | [38] | N | 20 | 20 | 12 | 12 | 0 | | 0.0 | 260 |
| 39 | [19] | N | 22 | 10 | 9 | 9 | 5 | 80 | 0.0 | 443 |
| 40 | [19] | N | 22 | 22 | 16 | 16 | 11 | 80 | 0.0 | 443 |
| 41 | [19] | N | 22 | 40 | 32 | 32 | 20 | 80 | 0.0 | 430 |
| 42 | [30] | N | 25 | 25 | 12 | 12 | 12 | 95 | −1.0 | 598 |
| 43 | [19] | N | 40 | 10 | 9 | 9 | 11 | 80 | 0.0 | 443 |
| 44 | [39] | N | 40 | 20 | 10 | 10 | 10 | 40 | 0.0 | 508 |
| 45 | [19] | N | 40 | 22 | 16 | 16 | 11 | 80 | 0.0 | 430 |
| 46 | [19] | N | 40 | 40 | 32 | 32 | 20 | 80 | 0.0 | 430 |
| 47 | [35] | N | 50 | 50 | 16 | 16 | 25 | 380 | 0.0 | 384 |
| 48 | [19] | N | 80 | 10 | 9 | 9 | 5 | 80 | 0.0 | 430 |
| 49 | [19] | N | 80 | 22 | 16 | 16 | 11 | 80 | 0.0 | 430 |
| 50 | [19] | N | 80 | 40 | 32 | 32 | 20 | 80 | 0.0 | 420 |
| 51 | [40] | N | 80 | 40 | 20 | 20 | 20 | 40 | 0.0 | 541 |
| 52 | [35] | N | 100 | 50 | 16 | 16 | 25 | 380 | 0.0 | 360 |
| 53 | [41] | N | 160 | 80 | 40 | 40 | 40 | 20 | 0.0 | 516 |
| 54 | [34] | 3B | 6 | 6 | 4 | 4 | 3 | 42 | 0.0 | 550 |
| 55 | [34] | 3B | 12 | 12 | 8 | 8 | 6 | 84 | 0.0 | 550 |

[a] 3B, three point bending; N, normal force

loading & response ratio coefficient shows that the stress range is responsible for almost 100% of the fatigue damage because of the data translation to $r_{lr} = 0.5$, meaning the mean (i.e. maximum) value does not contribute any more. Note that loading & response ratio $r_{lr} = 0.5$ is conservative from design perspective but may use for locations involving lower values unnecessarily some design space, which could improve the local structural detail effectiveness. Yield strength $S_y$ hardly affects the fatigue resistance (Figure 10D), although a single data set with $S_y < 400$ MPa is at the scatter band upper bound. The loading type (i.e. $f_n$ and $m_b$ dependent stress gradient) is not explicitly incorporated, explaining why the normal force data are not perfectly aligned with the bending moment induced data (Figure 10E). Despite the same FAT class prescription, the cruciform joint fatigue resistance turns out to be smaller than the T-joint fatigue resistance (Figure 10F).

## 3.2 | Hot spot structural stress concept

The hot spot structural stress criterion $S_s$[8,9,44] is a local, linear elastic intact geometry parameter. Since the equilibrium equivalent far-field stress (Figure 1) is involved, the "local" nominal stress issue has been solved. The $t_b$, $t_c$, $l_w$, $h_w$, $a_n$, and $\rho$ affected self-equilibrating stress (Figure 2) is not considered. Since the self-equilibrating stress determines up to what extent the notch is load carrying, in terms of fatigue resistance the extremes have been defined: non-load carrying (NLC) and load carrying (LC); 2 FAT classes, 2 $S_s$-$N$ resistance curves. The structural detail still has to be considered in order to classify a weld notch as NLC or LC. Selection is based on engineering judgement if no prescription is available. The IIW has assigned FAT100 for steel as-welded double-sided T-joint and double-sided cruciform joint fatigue resistance in air in case failure is base

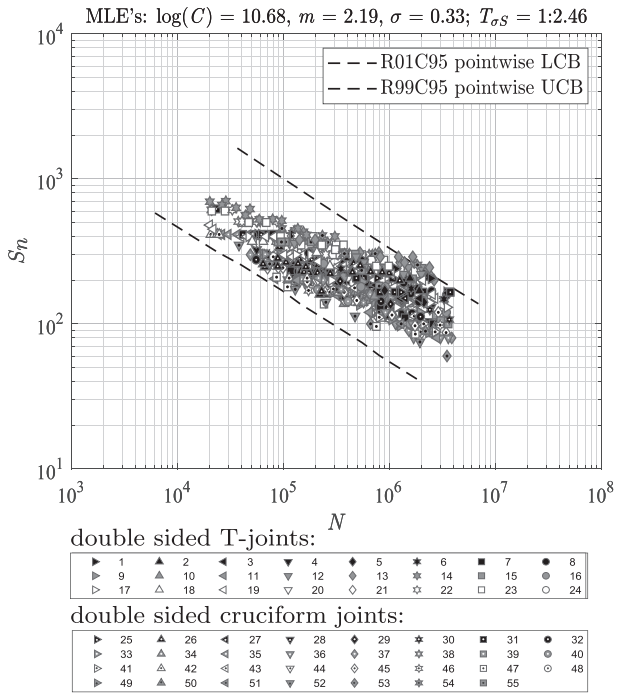


**FIGURE 9** Nominal stress based fatigue resistance without size and loading & response ratio corrections

plate weld toe induced, meaning $S_s = 100$ MPa at $N = 2{\cdot}10^6$ cycles. Size effect corrections are still required since $S_s$ is principally a surface point criterion. Adopting a force and moment equilibrium-based through-thickness linearisation provides an opportunity to capture exact $S_s$ values.[45] Any offset or angular misalignments affecting the far-field stress should explicitly be included. Loading & response ratio and residual stress considerations remain unchanged in comparison with the nominal stress criterion. Generally speaking, a decreased life time estimate uncertainty is obtained because of reduced (strength) scatter. The structural response modelling time and local geometry and loading and response information increases on the other hand, increasing criterion complexity and effort.[11]

A plane strain FE solid model has been used to capture $S_s$, allowing for through-thickness linearisation in order to obtain exact values. Regression analysis provides the resistance curve parameter estimates (Figure 11A) as well as the performance indicators: $\sigma = 0.33$ and $T_{\sigma S_s} = 1{:}2.41$, an increase in comparison with the nominal stress concept results (Figure 10). Size and loading & response ratio corrections (Equations 13 and 14) are incorporated, meaning that another explanation has to be identified. For the bending moment data $S_n = S_s$. However, applying a normal force to the base plate of a double-sided T-joint showing non-symmetry with respect to $(t_b/2)$ introduces a base plate rotation. Typical grips of fatigue testing machines provide clamped boundary conditions, meaning free rotation is prevented for. Second-order bending stresses will be introduced and have been incorporated, explaining why $S_s > S_n$ and $\sigma$ and $T_{\sigma S_s}$ are increased. Since the IIW design curve includes 5% welding-induced misalignment, all the fatigue resistance data $S_s$ values include a bending stress component $0.05S_s$ for the sake of a fair comparison. However, the (bending moment) data are up to some extent still below the FAT100 curve (Figure 11E). Except the loading type effect (Figure 11F), the influence factors show hardly any difference in comparison with the nominal stress based results (Figure 10).

## 3.3 | Effective notch stress concept

The (as) weld(ed) notch radius is typically small ($\rho \to 0$), and the theoretical stress concentration is not fully effective, meaning a zone 1 peak stress as fatigue damage criterion $S_{max} = \sigma_{max}$ (Figure 2) would be too conservative. Adopting a micro- and meso-structural notch support hypothesis, an effective notch stress estimate $S_e = \Delta\sigma_e$ can be obtained by averaging the notch stress distribution along the (presumed) crack path over a material characteristic micro- and meso-structural length $\rho^*$ to obtain an effective one $S_e = \Delta\sigma_e = \Delta\sigma_{av}$[46,47]; a local intact geometry parameter and line equivalent point criterion. The zone 2 notch stress gradient contribution is included; a size effect. Alternatively, a (fictitious) effective notch radius $\rho_e = s \cdot \rho^*$ can be employed in order to obtain the corresponding notch stress range $S_e = \Delta\sigma_e = \Delta\sigma_{av} = \Delta\sigma_{max}(\rho_e)$ of the original geometry at once.[48,49] Notch support factor $s$ includes the geometry and loading & response contribution and depends predominantly on notch angle, notch shape, loading & response mode, response condition, and the adopted response criterion. Micro- and meso-structural length $\rho^*$ is loading & response level dependent in the MCF and HCF regions because of changing life time initiation and growth contributions. Typically $\rho^*$ is obtained in an implicit way. Using fatigue test data, $S_e$-$N$ curve parameters can be estimated using regression analysis. Assuming the data correlation is maximum for the actual $\rho^*$, its most likely value can be identified.

### 3.3.1 | Artificial notch radius-based effective notch stress estimate

A most likely $\rho_e$ (averaged) engineering value can be established directly as well. For engineering applications, one reference radius $\rho_r = \rho_e = 1$ [mm] has been proposed because of simplifications with respect to the original criterion; an average value for the finite life time range data as reflected in the involved fatigue resistance data.[50] The IIW has assigned FAT225 based on maximum principal stress for steel as-welded joint fatigue resistance in air, meaning $S_e = 225$ MPa at $N = 2 \cdot 10^6$ cycles. The $\rho_r$ values require plate thickness $t_p \geq 5$ mm because of artificial

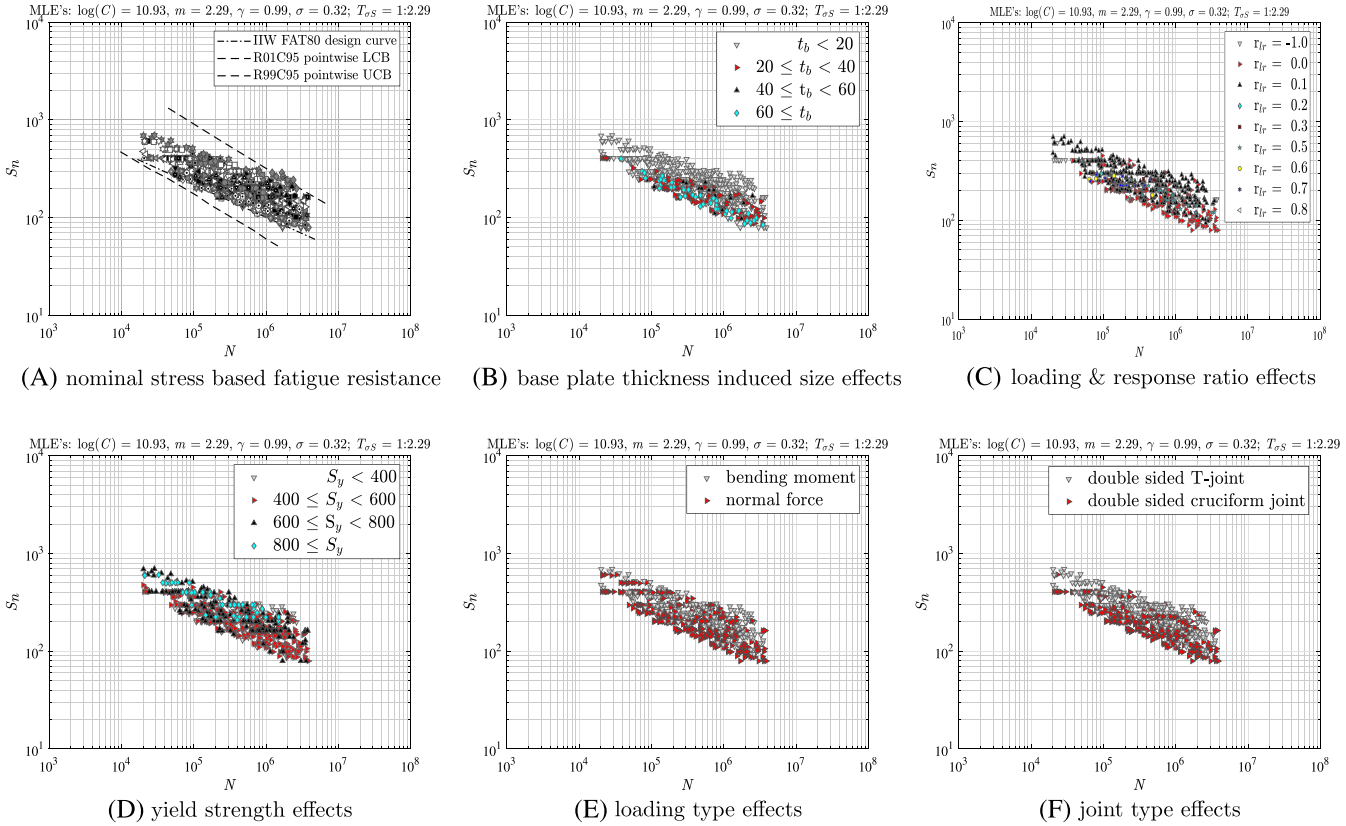


(A) nominal stress based fatigue resistance (B) base plate thickness induced size effects (C) loading & response ratio effects

(D) yield strength effects (E) loading type effects (F) joint type effects

**FIGURE 10** Nominal stress based fatigue resistance and influence factors [Colour figure can be viewed at wileyonlinelibrary.com]

cross-sectional weakening or strengthening at the weld notches, meaning structural stress corrections should be applied. Using an artificial notch radius to obtain an $S_e$ estimate has another limitation as well. Already 3 $\rho_r$ values: 1.0, 0.3, and 0.05 have been proposed for a particular range of $t_p$ values[51] and seems to be a first step to introduce a plate thickness-dependent value ($\rho/t_p$). The way offset and angular misalignments are incorporated and how the loading & response ratio as well as residual stress have been dealt with is similar to the procedure for the nominal and hot spot structural stress fatigue assessment concepts.[11]

Using plane strain FE solid models containing an artificial notch radius of 1 mm to obtain $S_e$, a logNormal distribution-based regression analysis provides the resistance curve parameter estimates (Figure 12) as well as the performance indicators: $\sigma = 0.26$ and $T_{\sigma S_e} = 1{:}1.65$. A significant improvement in comparison with the nominal stress and hot spot structural stress concept results is observed (Figures 10A and 11A). The loading & response ratio correction (Equation 14) is incorporated. In comparison with the IIW FAT225 curve, the regression analysis based one shows a similar slope $m$ but a larger intercept log($C$); FAT225 would provide non-conservative results.

### 3.3.2 | Stress averaging-based effective notch stress estimate

Typically, a solid FE solution is required to obtain a stress averaging-based effective notch stress estimate $S_e$. However, taking advantage of the weld notch stress distribution formulations (Equations 1 and 2), $S_e$ can be obtained for joints showing non-symmetry and symmetry with respect to half the plate thickness:

$$\begin{aligned}\sigma_e &= \frac{1}{\rho^*}\int_0^{\rho^*}\sigma_n(r)\mathrm{d}r \\ &= \sigma_s\cdot\left(\frac{t_p}{\rho^*}\right)\cdot\left\{\frac{1}{\lambda_s}\left(\frac{\rho^*}{t_p}\right)^{\lambda_s}\mu_s\lambda_s\left(\lambda_s+1\right)\right. \\ &\quad\times\left[\cos\left\{\left(\lambda_s+1\right)\beta\right\}-\chi_s\cos\left\{\left(\lambda_s-1\right)\beta\right\}\right] \\ &\quad+\frac{1}{\lambda_a}\left(\frac{\rho^*}{t_p}\right)^{\lambda_a}\mu_a\lambda_a\left(\lambda_a+1\right)\left[\sin\left\{\left(\lambda_a+1\right)\beta\right\}\right. \\ &\quad\left.-\chi_a\sin\left\{\left(\lambda_a-1\right)\beta\right\}\right] \\ &\quad\left.+C_{bw}\cdot\left\{\left(\frac{\rho^*}{t_p}\right)^2-\left(\frac{\rho^*}{t_p}\right)\right\}-r_s\cdot\left(\frac{\rho^*}{t_p}\right)^2\right\}\end{aligned} \tag{15}$$

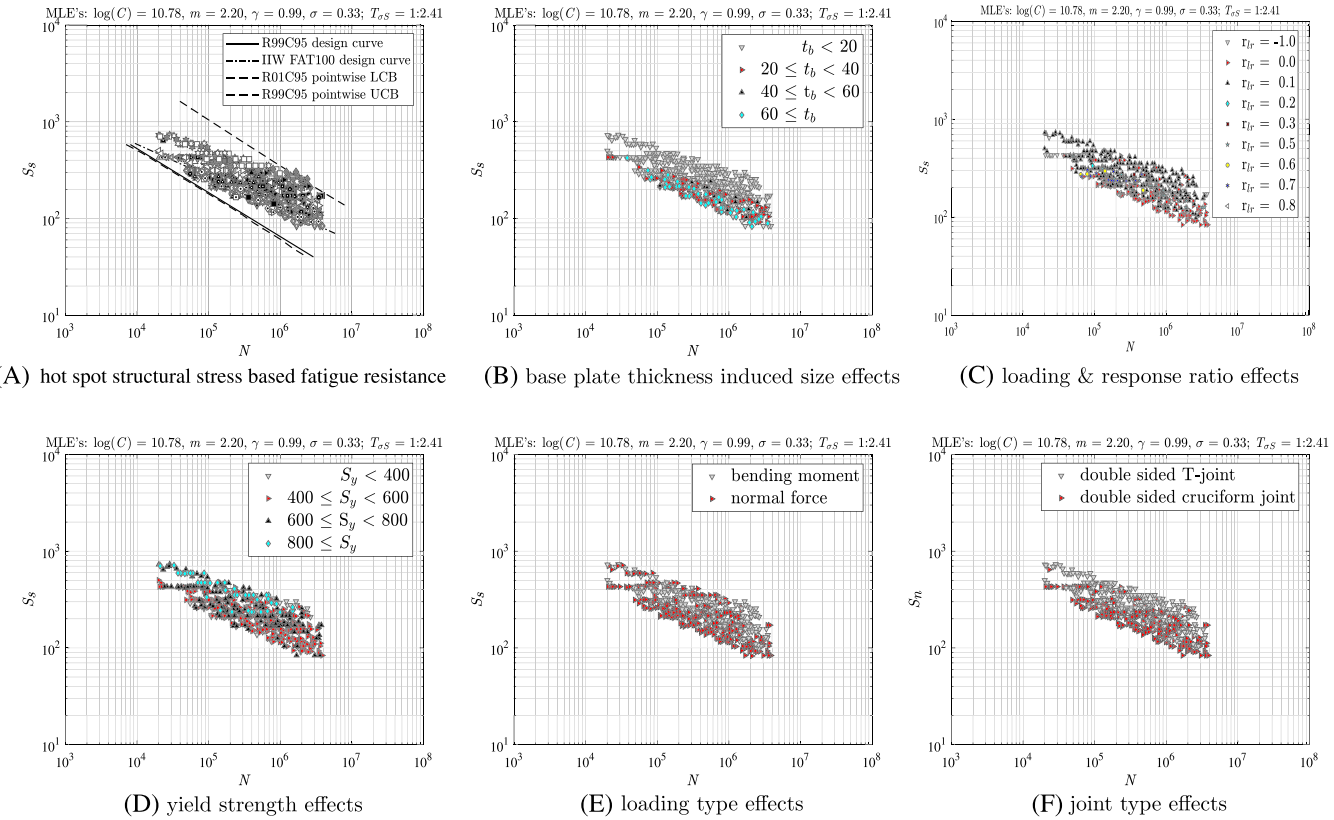


(A) hot spot structural stress based fatigue resistance (B) base plate thickness induced size effects (C) loading & response ratio effects

(D) yield strength effects (E) loading type effects (F) joint type effects

**FIGURE 11** Hot spot structural stress-based fatigue resistance and influence factors [Colour figure can be viewed at wileyonlinelibrary.com]

and

$$\begin{aligned}\sigma_e &= \frac{1}{\rho^*}\int_0^{\rho^*}\sigma_n(r)\mathrm{d}r \\ &= \sigma_s\cdot\left(\frac{t_p}{\rho^*}\right)\cdot\left\{\left[1-2r_s\left\{1-f\left(\frac{r}{t_p}=\frac{1}{2}\right)\right\}\right]\cdot\right. \\ &\quad\left(\frac{1}{\lambda_s}\left(\frac{\rho^*}{t_p}\right)^{\lambda_s}\mu_s\lambda_s\left(\lambda_s+1\right)\left[\cos\left\{\left(\lambda_s+1\right)\beta\right\}\right.\right. \\ &\quad\left.-\chi_s\cos\left\{\left(\lambda_s-1\right)\beta\right\}\right]+\frac{1}{\lambda_a}\left(\frac{\rho^*}{t_p}\right)^{\lambda_a}\mu_a\lambda_a\left(\lambda_a+1\right) \\ &\quad\times\left[\sin\left\{\left(\lambda_a+1\right)\beta\right\}-\chi_a\sin\left\{\left(\lambda_a-1\right)\beta\right\}\right] \\ &\quad\left.+C_{bw}\cdot\left\{2\left(\frac{\rho^*}{t_p}\right)^2-\left(\frac{\rho^*}{t_p}\right)\right\}\right) \\ &\quad+r_s\cdot\left\{2\cdot f\left(\frac{r}{t_p}=\frac{1}{2}\right)-1\right\} \\ &\quad\left.\times\left[\left\{1-f\left(\frac{r}{t_p}=\frac{1}{2}\right)\right\}\cdot\left(\frac{\rho^*}{t_p}\right)-\left(\frac{\rho^*}{t_p}\right)^2\right]\right\}.\end{aligned} \tag{16}$$

Plate thickness $t_p = t_b$ for base plate related notches. Material characteristic length $\rho^*$ information is required. A typical value $\rho^* = 0.4$ can be adopted, although plate thickness-dependent values are often obtained,[47,52,53] like for $\rho_r$. Since $\rho^*$ is assumed to be a material parameter, $t_p$ dependent welding procedures influencing the local material properties may explain the results. The effective notch stress hypothesis might be incomplete as well. Using the weld notch stress formulations (Equations 15 and 16 ), a different value is expected anyway since the maximum principal stress or Von Mises stress is not involved, and a $\rho^*$ estimate has been obtained using regression analysis; an average value for the considered fatigue resistance data (Figure 13A).

In comparison with the artificial notch radius-based results (Figure 12), the performance is improved since $\sigma = 0.23$ and could be a result of the artificial stiffness increase not being involved and the constant 1-mm notch radius may not be optimal considering the size (i.e. base plate thickness) effect. Scatter parameter $T_{\sigma S_e} \approx 1{:}1.52$ has been reduced as well. The most likely $\rho^* = 1.23$ seems reasonable, i.e. is larger than the typical value of 0.4 and is at the same time in between the thin and thick plate estimates.[52] The loading & response ratio coefficient $\gamma$ estimate is similar as for the nominal stress and hot spot structural stress-based fatigue resistance formulation, suggesting that $r_{lr}$ affects not only the far-field stress region, but the notch stress dominated one as well.

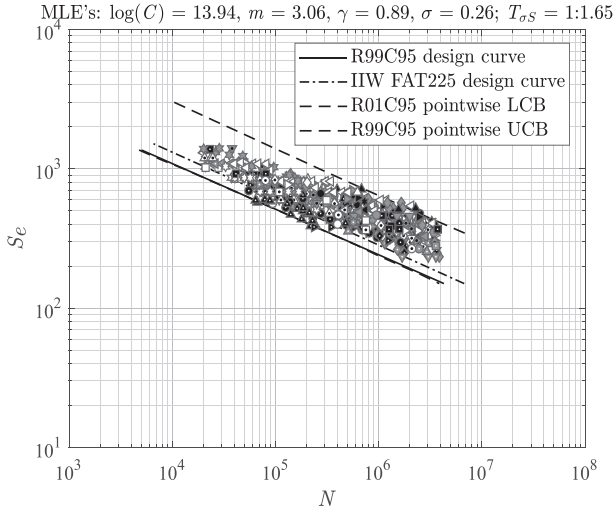


**FIGURE 12** Effective notch stress-based fatigue resistance with loading & response ratio correction, using an artificial notch radius

The influence factors (Figure 13B-F) show in comparison with the nominal stress concept and hot spot structural stress concept-based results an improved distribution over the data scatter band, in particular for the base plate thickness, the yield strength, loading type, and joint type effects. The actual weld notch stress distribution is explicitly involved, meaning the correct base plate stress gradient induced size effects are incorporated rather than approximated ones. The loading type is reflected in the weld notch stress distribution as well. The joint type shows the geometry (i.e. base plate thickness) and loading type information in one figure. Yield strength $S_y$ is not explicitly incorporated and the scatter hence a result of a better size and loading type description.

## 3.4 | Total stress concept

Assuming that arc-welded joints inevitably contain flaws, defects at the weld toe and weld root notches, fatigue damage at both locations will primarily be a matter of notch affected micro- and far-field dominated macrocrack growth, justifying a damage tolerant parameter life the stress intensity factor (Section 2). Cyclic loading & response turns $K$ into a crack growth driving force $\Delta K$, and defects may develop into cracks. The crack growth rate $(\mathrm{d}a/\mathrm{d}n)$ of micro-cracks emanating at notches show elastoplastic wake field affected anomalies. Modifying Paris' equation, a two-stage micro- and macro-crack growth relation similarity has been obtained and includes both the weld notch- and far-field characteristic contributions. Crack growth model integration provides a (MCF) single-slope resistance relation, a joint $S_T$-$N$ curve, correlating the life time $N$ and total stress fatigue damage criterion $S_T$; an area equivalent line criterion (Equation 17), capable to ensure small-scale specimen, large-scale specimen, and full-scale structure welded joint fatigue resistance similarity[7,11]:

$$S_T = \frac{\Delta\sigma_s}{(1-r_{lr})^{1-\gamma}\cdot I_N^{\frac{1}{m}}\cdot t_p^{\frac{2-m}{2m}}} \tag{17}$$

with

$$I_N = \int_{\frac{a_i}{t_p}}^{\frac{a_f}{t_p}} \frac{1}{\left\{Y_n\left(\frac{a}{t_p}\right)\right\}^n\cdot\left\{Y_f\left(\frac{a}{t_p}\right)\right\}^m\cdot\left(\frac{a}{t_p}\right)^{\frac{m}{2}}}\mathrm{d}\left(\frac{a}{t_p}\right).$$

Total stress criterion $S_T$ incorporates the effective structural stress range $\Delta\sigma_s/(1-r_{lr})^{1-\gamma}$ and scaling parameter $t_p^{2-m/2m}$ taking the response gradient-induced size effects into account. Notch crack growth integral $I_N$ requires an initial crack length. Adopting $(a_i/t_p) = C$ incorporates an average $t_p$ induced weld volume effect.

Maximum likelihood regression provides the most likely resistance curve parameter estimates (Figure 14 ). Performance indicators $\sigma = 0.22$ and $T_{\sigma S_T} = 1{:}1.47$ show an improvement in comparison with the averaged effective notch stress values (Figure 13).

In comparison with the values obtained for aluminium welded joints,[7] slope $m$ is similar since crack growth is the governing mechanism for both steel and aluminium. Elastoplasticity coefficient $n$ reflects non-monotonic crack growth and is similar as well since the same phenomena are involved for both steel and aluminium welded joints: notched geometry induced stress concentrations and welding induced residual stress. Investigation of the fatigue resistance performance parameters for varying initial crack length shows that the mean or most likely $(a_i/t_p) = 1\cdot10^{-2}$; a relatively large value. However, the performance sensitivity is low. For aluminium welded joints the most likely $(a_i/t_p) = 6\cdot10^{-3}$,[7] obtained involving double-sided T-joints, double/single-sided cruciform joints as well as double/single sided butt joints, double/single-sided attachments, etc. In general, welding of aluminium is considered to be more difficult than (low carbon) steel and a smaller $(a_i/t_p)$ for steel is expected. Since only double-sided T-joints and double-sided cruciform joints are involved at the moment, a more realistic value for steel has been adopted: $(a_i/t_p) = 1\cdot10^{-3}$. At the same time, the intercept $\log(C)$ ratio for steel and aluminium is still about a factor 3; i.e. approximately the ratio of the Young's moduli, the material bulk property in charge if the damage mechanism is crack growth dominated.

# 4 | CONCLUSIONS

For fatigue limit state design of arc-welded joints, the weld notch stress (intensity) distributions (Equations 1, 2,

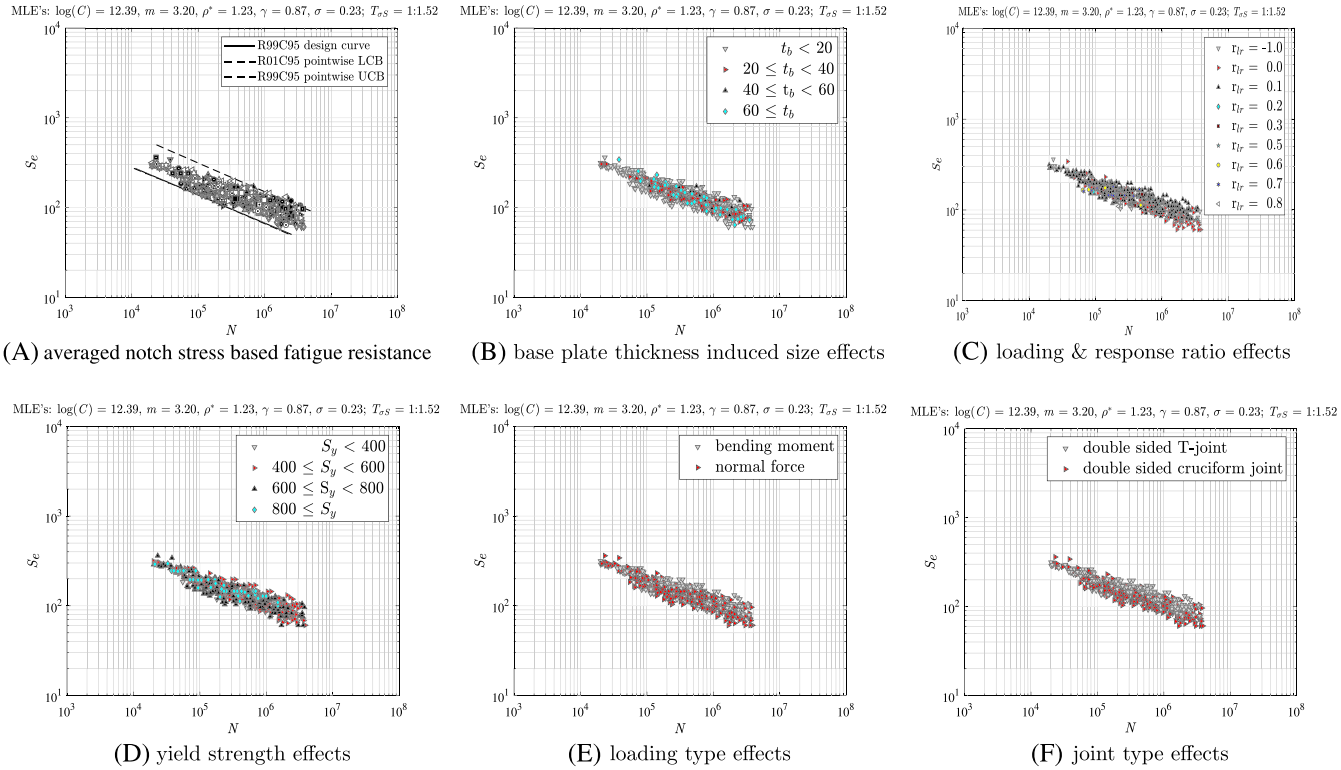


**FIGURE 13** Averaged effective notch stress-based fatigue resistance and influence factors [Colour figure can be viewed at wileyonlinelibrary.com]

and 10) contain essential information. The joint characteristic properties are particularly reflected in the involved weld load carrying stress component. Double weld FE beam models have been developed for double-sided T-joints and double-sided cruciform joints in order to obtain the weld load carrying stress coefficient $C_{bw}$, providing the required estimates and trends for varying geometry dimensions and loading and response combinations. Distinguishing a physical and fitting part, the model response has been investigated for respectively an applied normal force and bending moment, in order to identify the (physical) internal bending moments and normal forces providing a trend similar to the required $C_{bw}$. A fitting coefficient has been established to estimate the actual $C_{bw}$ value. As an alternative to the FE beam model $C_{bw}$ estimate, parametric fitting functions have been obtained as well, showing similar performance.

The weld notch stress (intensity) distributions formulations have been used to establish a total stress fatigue damage criterion and corresponding fatigue resistance curve; a total stress concept. Evaluating the total stress concept performance for welded double-sided T-joints and cruciform joints in steel marine structures in comparison with the nominal stress, hot spot structural stress, and effective notch stress, the total stress concept provides the most accurate fatigue design life time estimates. The strength scatter band index has reduced from $S_{\sigma S} = 1{:}2.46$ (nominal stress concept), $S_{\sigma S} = 1{:}2.41$ (hot spot structural stress concept), and $S_{\sigma S} = 1{:}1.52$ (effective notch stress concept) to $S_{\sigma S} = 1{:}1.47$ (total stress concept). Since a single-slope resistance curve is involved, the life time scatter band index can be obtained straightforward: $S_{\sigma N} = (S_{\sigma S})^m$, showing that the design life time estimate accuracy has increased from a factor $\sim$ 7.0 to $\sim$ 3.5; an improvement of $\sim$ 50%. Because of the involved total weld notch stress (intensity) distribution, in principle one joint fatigue resistance curve serves all welded joints. Comparing the artificial notch radius-based effective notch stress concept results with the stress averaging-based ones taking advantage of the weld notch stress distribution formulations improves the performance about 10%.

The performance of the nominal stress, hot spot structural stress, effective notch stress, and total stress concept shows that adding more local information to the fatigue damage criterion improves the fatigue life time estimate. The performance indicators seem to converge as well, suggesting that the life time estimate accuracy converges accordingly. To develop more advanced fatigue damage criteria involving more local information may not be attractive since the design life time estimate accuracy hardly improves, and the computational effort and concept complexity increase.

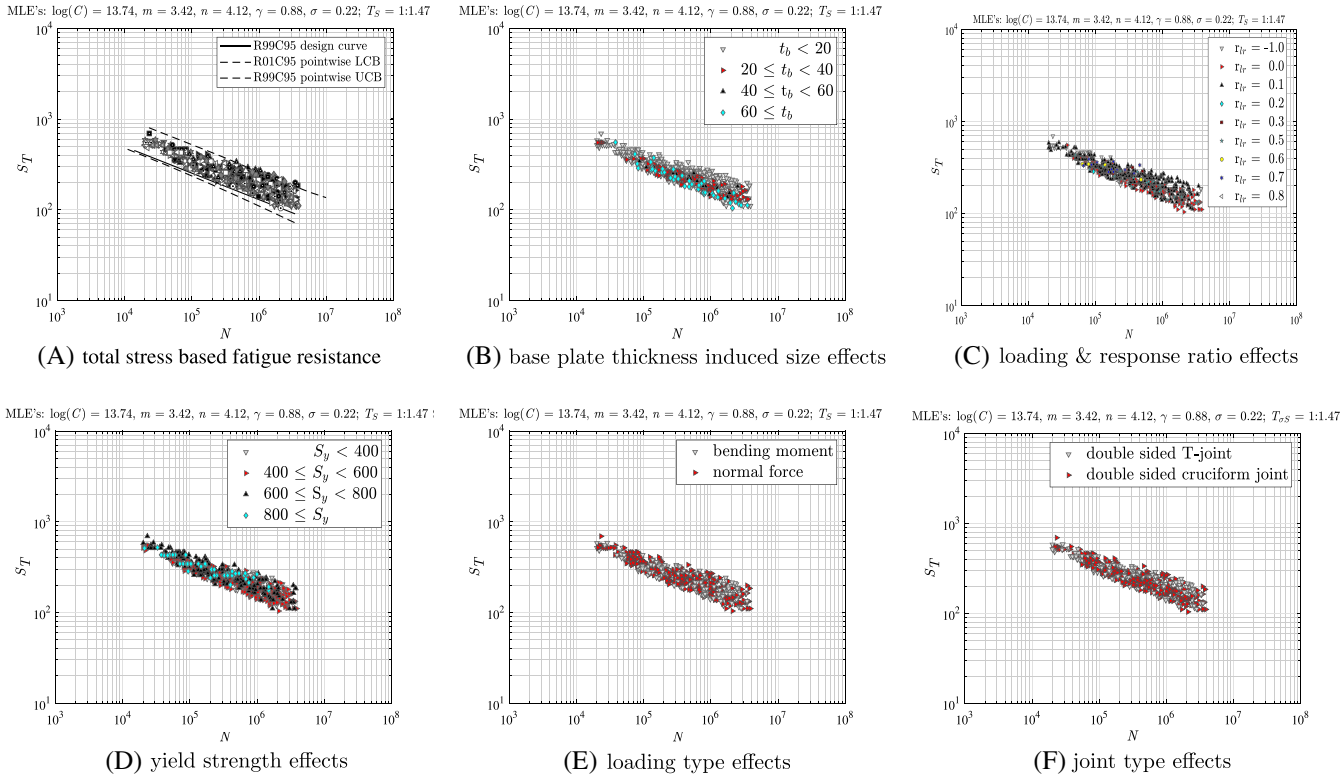


(A) total stress based fatigue resistance (B) base plate thickness induced size effects (C) loading & response ratio effects

(D) yield strength effects (E) loading type effects (F) joint type effects

**FIGURE 14** Total stress-based fatigue resistance and influence factors [Colour figure can be viewed at wileyonlinelibrary.com]


## ACKNOWLEDGEMENT

The financial support from the China Scholarship Council (grant number 201606950015) is gratefully acknowledged.



## ORCID

*Yanxin Qin* https://orcid.org/0000-0001-6048-4404
*Henk den Besten* https://orcid.org/0000-0002-8726-218X
*Saloni Palkar* https://orcid.org/0000-0002-5874-9116


## REFERENCES


1. Schijve J. *Fatigue of Structures and Materials*: Springer; 2009.
2. Franklin P. Fatigue design of oil tankers; a design approach. *Ph.D. Thesis*; 1993.
3. Müller L. Explanation for cracks in large container ships. *Schiff & Hafen*. 2003;12:30-31.
4. Ozguc O. Fatigue assessment of longitudinal stiffener end connections for ageing bulk carriers. *J Mar Sci Technol*. 2017;25(5):543-551.
5. Lillemäe I. Fatigue assessment of thin superstructure decks. *Ph.D. Thesis*; 2014.
6. Thomas GA, Davis MR, Holloway DS, Roberts TJ. The effect of slamming and whipping on the fatigue life of a high-speed catamaran. *Aust J Mech Eng*. 2006;3(2):165-174.
7. Den Besten JH. Fatigue resistance of welded joints in aluminium high-speed craft: a total stress concept. *Ph.D. Thesis*; 2015.
8. Hobbacher AF. *Recommendations for fatigue design of welded joints and components*: Springer; 2016.
9. CEN. Eurocode 3: Design of steel structures, part 1-9 fatigue. European Committee for Standardization; 2005.
10. DNV-GL. Classification notes No. 30.7 fatigue assessment of ship structures: DNV-GL; 2014.
11. Den Besten JH. Fatigue damage criteria classification, modelling developments and trends for welded joints in marine structures. *Ships and Offshore Structures*. 2018;13(8):787-808.
12. DNV-GL. Finite element analysis. DNV-GL; 2016.
13. Rörup J, Maciolowski B, Darie I. FE-based strength analysis of ship structures for a more advanced class approval. In: Proceedings of the 13th International Symposium on practical design of ships and other floating structures (prads 2016). Technical University of Denmark (DTU); 2016; Copenhagen.
14. Atzori B, Lazzarin P, Tovo R. From a local stress approach to fracture mechanics: a comprehensive evaluation of the fatigue strength of welded joints. *Fatigue Fract Eng Mater Struct*. 1999;22(5):369-381.
15. Lazzarin P, Tovo R. A unified approach to the evaluation of linear elastic stress fields in the neighborhood of cracks and notches. *Int J Fract*. 1996;78(1):3-19.
16. Pook LP. A 50-year retrospective review of three-dimensional effects at cracks and sharp notches. *Fatigue Fract Eng Mater Struct*. 2013;36(8):699-723.
17. Tada H, Paris PC, Irwin GR. The Stress Analysis of Cracks Handbook , New York: ASME Press; 2000.
18. Miki C, Mori T, Sakamoto K, Kashiwagi H. Size effect on the fatigue strength of transverse fillet welded joints. *J Struct Eng*. 1987;33:393-402.
19. SR202. *Fatigue design and quality control for offshore structures*. Japanese: Committee of Shipbuilding Research Association of Japan; 1991.
20. Galtier A, Statnikov ES, Irsid A. The influence of ultrasonic impact treatment on fatigue behaviour of welded joints in high-strength steel. *Weld in the World*. 2004;48(5-6):61-66.

21. Pedersen MM, Mouritsen OØ, Hansen MR, Andersen J, Wenderby J. Comparison of post-weld treatment of high-strength steel welded joints in medium cycle fatigue. *Weld in the World*. 2010;54(7-8):208-217.
22. Ahola A, Nykänen T, Björk T. Effect of loading type on the fatigue strength of asymmetric and symmetric transverse non-load carrying attachments. *Fatigue Fract Eng Mater Struct*. 2017;40(5):670-682.
23. Mecozzi E, Lecca M, Sorrentino S, et al. *Fatigue behaviour of high-strength steel-welded joints in offshore and marine systems (FATHOMS)*: Publication Office of the European Union; 2010.
24. Budano S, Kuppers M, Kaufmann H, Meizso AM, Davies C. Application of high-strength steel plates to welded deck components for ships and bridges subjected to medium/high service loads. *EUR*. 2007;22571.
25. Statnikov ES, Muktepavel VO, Blomqvist A. Comparison of ultrasonic impact treatment (UIT) and other fatigue life improvement methods. *Weld in the World*. 2002;46(3-4):20-32.
26. Haagensen PJ. IIW's round robin and design recommendations for improvement methods; 1997.
27. Noordhoek C, Scholte H, Jonkers P, Koning C, Dijkstra O. *Fatigue and fracture behavior of welded joints in high strength steel(Fe E 460)*: Office for official publications of the European Communities; 1993.
28. Stoschka M, Di Leitner M, Fössl T, Posch G. Effect of high-strength filler metals on fatigue. *Weld in the World*. 2012;56(3-4):20-29.
29. Leitner M, Stoschka M, Eichlseder W. Fatigue enhancement of thin-walled, high-strength steel joints by high-frequency mechanical impact treatment. *Weld in the World*. 2014;58(1):29-39.
30. Kihl DP, Sarkani S. Thickness effects on the fatigue strength of welded steel cruciforms. *Int J Fatigue*. 1997;19(93):311-316.
31. Nykänen T, Marquis G, Björk T. Effect of weld geometry on the fatigue strength of fillet welded cruciform joints. *Proceedings of the international symposium on integrated design and manufacturing of welded structures*. Lappeenranta: Lappeenranta University of Technology; 2007.
32. NIMS. Data sheets on fatigue strength of non-load-carrying cruciform welded joints of sm490b steel for welded structures-effect of plate thickness (patr 1, thickness 9 mm). NIMS Fatigue Datasheet No.96, National Research Institute for Metals; 2004.
33. Kuhlmann U, Bergmann J, Dürr A, et al. Erhöhung der ermüdungsfestigkeit von geschweißten höherfesten baustählen durch anwendung von nachbehandlungsverfahren. *Stahlbau*. 2005;74(5):358-365.
34. Lindqvist J. Fatigue strengths thickness dependence in welded construction. *Ph.D. Thesis*; 2002.
35. Maddox SJ. *The effect of plate thickness on the fatigue strength of fillet welded joints*: The Welding Institute; 1987. ISBN: 0853002088.
36. NIMS. Data sheets on fatigue strength of non-load-carrying cruciform welded joints of sm570q steel for welded structures. NIMS Fatigue Datasheet No.90, Tokyo: National Research Institute for Metals; 2002.
37. NIMS. Data sheets on fatigue strength of non-load-carrying cruciform welded joints of sm490b steel for welded structures-effect of residual stress. NIMS Fatigue Datasheet No.91, Tokyo: National Research Institute for Metals; 2003.
38. Kudryavtsev Y, Kleiman J, Lugovskoy A, et al. Rehabilitation and repair of welded elements and structures by ultrasonic peening. *Weld in the World*. 2007;51(7-8):47-53.
39. NIMS. Data sheets on fatigue strength of non-load-carrying cruciform welded joints of sm490b steel for welded structures-effect of plate thickness (patr 4, thickness 40 mm). NIMS Fatigue Datasheet No.114, Tokyo: National Research Institute for Metals; 2011.
40. NIMS. Data sheets on fatigue strength of non-load-carrying cruciform welded joints of sm490b steel for welded structures-effect of plate thickness (patr 3, thickness 80 mm) . NIMS Fatigue Datasheet No.108, Tokyo: National Research Institute for Metals; 2009.
41. NIMS. Data sheets on fatigue strength of non-load-carrying cruciform welded joints of sm490b steel for welded structures-effect of plate thickness (patr 2, thickness 160 mm). NIMS Fatigue Datasheet No.99, Tokyo: National Research Institute for Metals; 2006.
42. Dekking FM, Kraaikamp C, Lopuhaä HP, Meester LE. *A Modern Introduction to Probability and Statistics: Understanding Why and How*. London: Springer-Verlag; 2005.
43. Walker K. The effect of stress ratio during crack propagation and fatigue for 2024-t3 and 7075-t6 aluminum. *Effects of environment and complex load history on fatigue life*: ASTM International; 1970.
44. Niemi E, Fricke W, Maddox SJ. *Fatigue Analysis of Welded Components—Designer's Guide to the Structural Hot Spot Stress approach*. Cambridge: Woodhead Publishing Limited; 2006.
45. Dong P. A structural stress definition and numerical implementation for fatigue analysis of welded joints. *Int J Fatigue*. 2001;23:865-876.
46. Neuber H. *Kerbspannungslehre*: Springer-Verlag; 1937.
47. Zhang G, Sonsino CM, Sundermeier R. Method of effective stress for fatigue: Part ii–applications to v-notches and seam welds. *Int J Fatigue*. 2012;37:24-40.
48. Sonsino CM, Fricke W, de Bruyne F, et al. Notch stress concepts for the fatigue assessment of welded joints-background and applications. *Int J Fatigue*. 2012;34:2-16.
49. Radaj D, Lazzarin P, Berto F. Generalised neuber concept of fictitious notch rounding. *Int J Fatigue*. 2013;51:105-115.
50. Rother K, Rudolph J. Fatigue assessment of welded structures: practical aspects for stress analysis and fatigue assessment. *Fatigue Fract Eng Mater Struct*. 2011;34(3):177-204.
51. Rother K, Fricke W. Effective notch stress approach for welds having low stress concentration. *Int J Press Vessel Pip*. 2016;147:12-20.
52. Baumgartner J, Waterkotte R. Crack initiation and propagation analysis at welds assessing the total fatigue life of complex structures. *Mater Werkst*. 2015;46(2):123-135.
53. Liinalampi S, Remes H, Lehto P, et al. Fatigue strength analysis of laser-hybrid welds in thin plate considering weld geometry in microscale. *Int J Fract*. 2016;87:143-152.


**How to cite this article:** Qin Y, den Besten H, Palkar S, Kaminski ML. Fatigue design of welded double-sided T-joints and double-sided cruciform joints in steel marine structures: A total stress concept. *Fatigue Fract Eng Mater Struct*. 2019;42:2674–2693. https://doi.org/10.1111/ffe.13089